PCCP

ROYAL SOCIETY OF CHEMISTRY

PAPER

View Article Online
View Journal | View Issue

Cite this: *Phys. Chem. Chem. Phys.*, 2025, **27**, 4152

Systematic study of the structural, energetic and elastic properties of $U_{1-y}Am_yO_{2-x}$ compounds using empirical interatomic potentials

Baptiste Labonne, [a] Christine Guéneau[b] and Marjorie Bertolus*[a]

Uranium–americium mixed oxides are envisaged as fuels or blankets for the transmutation of americium in fast neutron reactors, which requires an accurate knowledge of their properties. Here, the Cooper–Rushton–Grimes (CRG) potential terms related to Am^{4+} are reoptimized to lower the very high melting temperature of AmO_2 predicted by the potential (≈3350 K) while keeping other properties unchanged. The resulting terms are used alongside U^{4+} parameters as well as previously optimized terms for the Am^{3+} and U^{5+} oxidation states in combination with molecular dynamics to perform a systematic study of the structural, thermodynamic and elastic properties of hypostoichiometric uranium–americium mixed oxides $U_{1-y}Am_yO_{2-x}$ with $0 \leq y \leq 1$ and $0 \leq x \leq 0.1$ over a wide temperature range (250–4500 K). The properties calculated include the lattice parameter and related properties (density, thermal expansion coefficient), the enthalpy increment and related properties (specific heat capacity, enthalpy of fusion), the melting temperature and the elastic constants. Our study shows a peculiar evolution of properties with the americium content with a change in the evolution for 50% americium due to the various oxidation states of the cations present in these compounds. Results presented in this paper provide significant insight into the properties of uranium–americium mixed oxides for all compositions, in particular for high americium contents, non-stoichiometric oxides and at high temperature and complement the few experimental data available for these materials.

Received 2nd October 2024,
Accepted 28th January 2025

DOI: 10.1039/d4cp03797a

rsc.li/pccp

I. Introduction

Uranium–americium mixed oxides are envisaged as fuels or blankets in fast neutron reactors to allow for the transmutation of americium in view of the reduction of its quantity in nuclear waste.[1] In this context, the knowledge of thermodynamic, structural and elastic properties of $(U,Am)O_2$ fuels is of crucial importance for fuel manufacturing, as well as for safe reactor operation. Beyond the use of low americium content fuel in reactor, highly Am-enriched uranium–americium oxides are being considered for space applications in radioisotope thermoelectric generators.[2–10] The knowledge of thermodynamic properties for all Am contents, including high ones, is therefore crucial. In addition, the knowledge of elastic properties, in particular the elastic constants C_{11}, C_{12} and C_{44}, is necessary since these are direct parameters of micromechanical laws for single crystals, which are then homogenised for the simulation of the behaviour of the polycrystalline material.

Experimental investigations on americium-bearing compounds are difficult due to the high radioactivity of this element and the data reported in the literature on uranium–americium oxides are relatively scarce. The U–Am–O ternary phase diagram data were obtained by Horlait *et al.*,[11] Vălu *et al.*,[12] Prieur *et al.*,[13–15] Lebreton *et al.*[16] and more recently Epifano *et al.*[17–20] A CALPHAD model of the ternary system was then developed by Epifano *et al.* using these experimental data.[21] This work pointed out that further investigations of this system are required, especially for high Am contents and oxygen to metal ratio (O/M) below 2 to improve the CALPHAD modelling of americium-bearing mixed actinide oxides.

Atomic scale modelling has proved itself to be an important complement to experimental characterizations to obtain data and bring insight into the behaviour of fuel materials over a wide range of compositions and conditions.[22,23] We use it in this study to complement the few experimental data available on uranium–americium oxides.

The Cooper–Rushton–Grimes (CRG) potential[24] has yielded excellent results on several pure and mixed actinide oxides,[25–37] and was adapted for the study of uranium–americium mixed oxides in a previous paper.[38] It yields, however, a very high melting temperature for AmO_2 (≈3350 K), which could impact the results on uranium–americium mixed oxides with high Am content. We propose here an estimate of the probable melting temperature range for a hypothetical americium dioxide based on

[a] *CEA, DES, IRESNE, DEC, Cadarache, F-13108 Saint-Paul-Lez-Durance, France. E-mail: marjorie.bertolus@cea.fr*
[b] *Université Paris-Saclay, CEA, S2CM, Service de recherche en Corrosion et Comportement des Matériaux, 91191 Gif-sur-Yvette, France*

thermodynamic considerations and compare it to the very scarce data available.[39,40]

Based on this range estimate, we reoptimized the interaction terms related to Am^{4+} to lower the AmO_2 melting temperature while keeping structural, thermodynamic and elastic properties virtually unchanged, as they are in line with experimental data. We then used the updated parameters in combination with U^{4+}, Am^{3+} and U^{5+} terms to calculate the structural, thermodynamic and elastic properties of $U_{1-y}Am_yO_{2-x}$ with $0 \leq y \leq 1$ and $0 \leq x \leq 0.1$.

The paper is organized as follows. We briefly recall the potential formalism and calculation details, which are presented in detail in the paper dedicated to the optimization of the Am^{3+} and U^{5+} terms.[38] We then describe precisely the method used to include the melting temperature in the fitting procedure and the generation scheme used to incorporate vacancies in our supercells. We then present and discuss the results of the systematic study of $U_{1-y}Am_yO_{2-x}$ compounds: the structural and energetic properties extracted directly from simulations, the derivative properties, *i.e.*, thermal expansion coefficient and specific heat capacity, the melting temperatures, and the elastic properties. Finally, we conclude and present the outlooks of this work.

II. Methods

II.A. Potential formalism

The Cooper–Rushton–Grimes (CRG) potential[24] is an embedded atom method (EAM) potential[41,42] with the following formal definition for the potential energy of an atom i as follows:

$$E_i = \frac{1}{2}\sum_{j\neq i}\varphi_{\alpha\beta}(r_{ij}) - G_\alpha\sqrt{\sum_{j\neq i}\sigma_\beta(r_{ij})} \quad (1)$$

The first term is the pair potential, where $\varphi_{\alpha\beta}(r_{ij})$ is the sum of the long-range Coulomb and of the short-range Morse[43] and Buckingham[44] potentials. The second term is the N-body contribution representing the embedding energy of the atom i in the electronic density owing to its neighbours, enabling one to take into account the impact of the atomic environment on the potential energy of the atom i.

This potential formalism is remarkably good at reproducing known properties of actinide oxides, in particular the lattice parameter, the Cauchy violation of the elastic constants $C_{12} \neq C_{44}$ and the bulk modulus temperature dependence, probably due to the strongly ionic iono-covalent bonding in these systems. The terms originally published were optimized on experimental lattice parameters and elastic properties, while ensuring that fluorite was the most stable structure. The terms subsequently added for Am^{3+} and U^{5+} were optimized using lattice parameters and enthalpy increments[12,17] for several stoichiometric uranium–americium mixed oxides at room temperature[11,16] and at 1000 K.[16,19]

II.B. Calculation details

II.B.1. Building the supercells. The compositions studied in this paper are $U_{1-y}Am_yO_{2-x}$ with $0 \leq y \leq 1$ and $0 \leq x \leq 0.1$. As in our previous study,[38] the uranium–americium mixed oxides supercells were generated using a custom Python script computing pair distances by positioning cations as homogeneously as possible and Am^{3+} and U^{5+} as close as possible to each other. One hundred configurations were generated for each composition. The five most homogeneous ones were chosen from the computation of the distances between the various cations and used in production runs. The size of the supercells depends on the properties calculated (see next section). The concentrations of the cations with various oxidation states determined by electronic structure calculations[45] are represented in Fig. 1 for compounds with oxygen to metal ratio O/M = 2.00. It can be seen that Am^{4+} cations are present only for compositions with Am/(Am + U) > 0.5. This specific behaviour of $(U,Am)O_{2\pm x}$ was observed experimentally by Epifano *et al.*, who measured the multi-valence states in the mixed oxides using XAS.[18] The CALPHAD model, derived from experimental oxygen potential and phase diagram data, reproduces this trend as well.[21]

For the study of hypostoichiometric oxides, oxygen vacancies were introduced randomly considering their relatively low concentration and the possibility for oxygen to diffuse. Moreover, DFT+U calculation results on AmO_{2-x} showed that configurations with oxygen vacancies nearest neighbours to Am^{3+} were not necessarily the most stable.[46] The charge neutrality was ensured by the reduction of one or several species. The order in which species are reduced is known from DFT+U calculations:[45]

- Below 50% Am, only U^{5+} can be reduced to U^{4+} since all americium cations are already in the (+III) oxidation state and U^{3+} terms are not included in the potential. This implies that there is a limit on the oxygen to metal ratio imposed by the americium content.
- Above 50% Am, Am^{4+} ions are reduced first to Am^{3+}, followed by U^{5+} ions to U^{4+} if necessary. The latter occurs only for large deviations from stoichiometry for $0.50 < Am/(Am + U) \leq 0.60$.

II.B.2. Determination of structural, thermodynamic and elastic properties. All calculations are performed using the large-scale atomic/molecular massively parallel simulator (LAMMPS) code.[47]

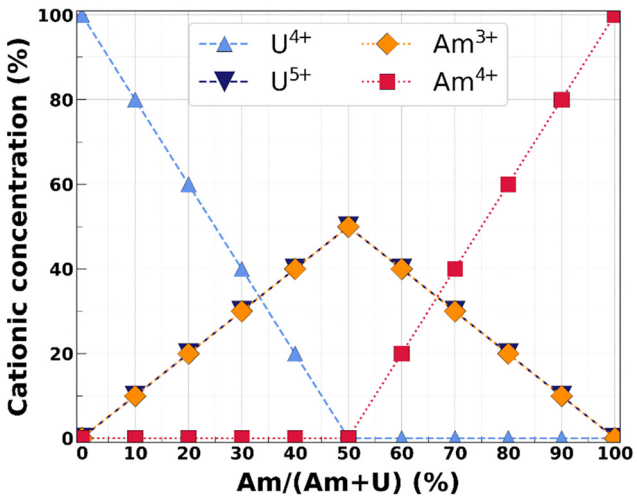

Fig. 1 Concentrations of the various cationic oxidation states in $(U,Am)O_2$ compounds as a function of americium content, reproduced from ref. 45.

II.B.2.a. Heat until it melts and moving interface methods. The Heat Until it Melts (HUM)[48,49] and moving interface (MI)[50,51] methods are presented in detail in our previous paper, only the main points are recalled here. The HUM method allows for the determination of the structural and energetic properties of interest as a function of temperature. We equilibrated the supercells for 100 ps in the NPT ensemble at 0 bar (as is standard in the community given the negligible pressure dependence of studied properties and to ensure $U = H$), from 250 K to 4500 K every 25 K, and averaged the properties over the last 50 ps for each temperature. These simulations were performed on $6 \times 6 \times 6$ replications of the conventional fluorite cell, *i.e.*, 2592-atom supercells for stoichiometric systems.

Due to overheating effects caused by the finite-size of the system, the melting temperature detected in a HUM run is overestimated by approximately 20%.[52,53] The MI method is thus used to estimate a pseudo-melting temperature by simulating a solid–liquid interface, imposing the final temperature and pressure and monitoring the position of the interface. This monitoring was performed by computing the local entropy and the centro-symmetry parameter, as well as performing common neighbour analyses using LAMMPS to obtain the profile of these properties along the longest dimension of the supercell. The position of the interface at the end of the simulation indicates if the applied temperature is above or below the melting temperature yielded by the potential. The melting temperature is found when at the end of the simulation, both phases account for approximately half the supercell each. These simulations were performed in the NPT ensemble with a 25 K temperature step and 1 ns final relaxation time on $8 \times 8 \times 16$ replications of the conventional fluorite cell, *i.e.*, 12 288-atom supercells for stoichiometric compounds.

For both types of calculations, we used a 1 fs timestep, a 0.1 ps temperature damping parameter and a 0.5 ps pressure damping parameter for the Nosé–Hoover thermostat and barostat, respectively. Simulations were performed on five supercells with varying random configurations of U and Am positions in the cationic sublattice for each composition and on three seeds for the initialization of the velocities per supercell, totalling fifteen repetitions for a given set of conditions. Properties were then averaged over these simulations, taking twice the standard deviation as the uncertainty.

II.B.2.b. Calculation of elastic properties. The supercells equilibrated at a finite temperature for a given pressure using the HUM method can be used to compute the elastic constants. To do so, small deformations are applied to the simulation cell. These must be small enough so that the stress *versus* strain relationship respects Hooke's law, *i.e.*, remains linear. This allows for the determination of the elastic tensor which, in the case of cubic materials, is entirely described by the C_{11}, C_{12} and C_{44} constants using the Voigt notation. These can be used to compute various elastic moduli, as well as the Zener ratio, which measures the isotropy of cubic materials, in the Voigt–Reuss–Hill (VRH) scheme,[54–56] therefore yielding a complete representation of the linear elastic properties of the material.

In practice, we used the lattice parameters yielded by the HUM method every 100 K to rescale the perfect supercell at each temperature before performing a $2 \times 2 \times 2$ replication due to the sensibility of elastic properties on the supercell size. We then equilibrated the resulting $12 \times 12 \times 12$ replication supercell at the corresponding temperature and zero pressure in the NPT ensemble for 30 ps to dislodge atoms from their equilibrium position. The LAMMPS "ELASTIC_T" script was used on the resulting structure to apply a $\pm 4\%$ deformation successively along all crystallographic axes and tilt factors in order to compute C_{11}, C_{12} and C_{44}. The Zener ratio A is then calculated as:

$$A = \frac{2C_{44}}{C_{11} - C_{12}} \quad (2)$$

As for the previous types of calculations, we used a 1 fs timestep, a 0.1 ps temperature damping parameter and a 0.5 ps pressure damping parameter for the Nosé–Hoover thermostat and barostat, respectively. Simulations were performed on five supercells with varying uranium and americium positions for each composition. Properties were then averaged, taking twice the standard deviation across the five simulations as the uncertainty.

III. Reoptimization and validation of Am^{4+} related potential parameters

III.A. Estimated melting temperature range

A single experimental value of AmO_2 melting temperature was published by McHenry in 1965.[57] The measurement was performed without control of the oxygen content and yielded 2386 K at standard pressure. CALPHAD-based calculations[58,59] and experimental characterizations,[17,58] however, show that the reduction process of AmO_2 begins at temperatures as low as 1100 K. The calculated phase diagram also indicates that the melting should occur for an O/M ratio of approximately 1.76. The melting temperature of stoichiometric americium dioxide can therefore only be estimated. Casalta estimated the melting temperature of AmO_2 at 2520 K without providing the method.[39] More recently, Kato *et al.* proposed a value of 2773 K[40] based on the effect of Am on the melting temperature of mixed actinide oxides.

The melting temperature of stoichiometric americium dioxide predicted by the CRG potential using the MI method is about 3350 K. Since the melting temperature of AmO_2 seems to have a strong influence on that of the mixed uranium–americium oxides with high Am contents[60] and as a starting point for the precise modelling of AmO_{2-x} compounds, a reoptimization of the Am^{4+} related parameters of the potential is needed to lower this value. We propose here a method to determine a probable melting temperature interval for a hypothetical stoichiometric AmO_2. We use the enthalpy of formation and Gibbs free energy of formation of the actinide dioxides to infer the stability of these compounds. Using values from,[61,62] we compute the ratios $T_m/\Delta_f H^\circ$ and $T_m/\Delta_f G^\circ$ for all actinide dioxides in the series ThO_2 to AmO_2. Results are reported in Table 1 and shown in Fig. 2. It is observed that the values are similar for all actinide dioxides except for AmO_2, giving an additional hint that the experimental value by McHenry was not obtained on the stoichiometric compound.

Table 1 Computed ratios $T_m/\Delta_f H^\circ$ and $T_m/\Delta_f G^\circ$ for actinide dioxides

	ThO_2	PaO_2	UO_2	NpO_2	PuO_2	AmO_2
$T_m/\Delta_f H^\circ$ (K mol kJ^{-1})	−2.977	−2.891	−2.876	−2.848	−2.858	−2.560
$T_m/\Delta_f G^\circ$ (K mol kJ^{-1})	−3.123	−3.036	−3.024	−3.007	−3.023	−2.721

Considering the various degrees of uncertainty associated to these ratios, a simple linear fit on the values of other actinide dioxides is used to determine a probable upper limit for these two ratios for americium dioxide. Values obtained are −2.81 K mol kJ^{-1} and −2.97 K mol kJ^{-1} for $T_m/\Delta_f H^\circ$ and $T_m/\Delta_f G^\circ$, respectively, corresponding to a melting temperature of 2620 K and 2605 K, respectively. The latter is chosen as the lower bound for our melting temperature interval estimate.

The lower limit for these two ratios, which corresponds to the upper limit of the temperature interval, is more difficult to assess due to the transition in the chemical nature of cation-oxygen bonds taking place between plutonium and neptunium dioxides.[63,64] It can be seen that the value of the two ratios decreases slightly from NpO_2 to PuO_2, but we have no indication on their behaviour for heavier actinides. We thus take the extreme values, *i.e.*, those of ThO_2, as being the lower limit for AmO_2. The corresponding melting temperatures are 2780 K and 2735 K for $T_m/\Delta_f H^\circ$ and $T_m/\Delta_f G^\circ$, respectively.

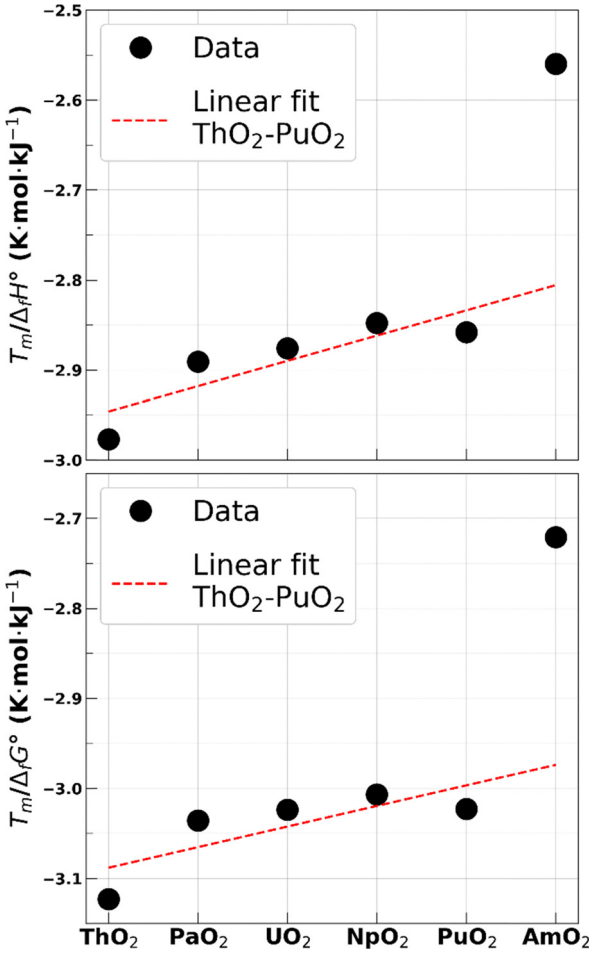

Fig. 2 Ratios $T_m/\Delta_f H^\circ$ (top) and $T_m/\Delta_f G^\circ$ (bottom) for the actinide dioxides series.

We thus consider that the melting temperature of a hypothetical americium dioxide is in the 2605–2780 K range. This rule of thumb gives results in line with the previous evaluations while diminishing the width of the interval spanned by the previous two estimates by Casalta and Kato *et al.* cited above. Despite the large uncertainties in this evaluation, it is clear that the current CRG potential largely overestimates the melting temperature of a hypothetical stoichiometric americium dioxide.

III.B. Fitting procedure

We used the DAKOTA software[65] to reoptimize the potential parameters in order to lower the melting temperature of americium dioxide while keeping other properties such as the room-temperature lattice parameter and bulk modulus, the thermal expansion and the enthalpy increment unchanged, as they are in excellent agreement with the available experimental data. Based on previous work by Cooper *et al.* to lower the melting temperature of PuO_2 predicted by the original potential parameters,[25] we largely increased the N-body parameters of Am^{4+} while adjusting the Am^{4+}–O terms to ensure that other properties were changed as little as possible. We employed the single-objective genetic algorithm (SOGA) using the JEGA package[66] implemented in DAKOTA to optimize all parameters simultaneously, running the optimisation with five different initialisation seeds. Properties were calculated as follows: (1) room-temperature lattice parameter, (2) room-temperature bulk modulus, (3) melting temperature, (4) lattice parameter and enthalpy increment at 1000 K. After each step, the result was examined and the set of parameters was discarded if the computed properties were unacceptably far from their reference value. The tolerance for each property was chosen large enough to leave space for the subsequent optimization of the parameters, while rejecting sets having no chance of converging towards a valid solution. Values used for the optimization as well as tolerance criteria are reported in Table 2.

We used several loss functions to guide the optimization: first the absolute relative error on numerical properties and second a 0 or 1 value corresponding to the identification of the solid to liquid phase transition or not, respectively. We applied various weights to the linear combination of these loss functions to find the best set of parameters. A weight value of 5 was chosen for the loss function regarding each room-temperature lattice parameter, bulk modulus and 1000 K lattice parameter. A weight value of 1 was used for the loss function of the enthalpy increment due to the rather high rigidity of the potential formalism with regard to energetic properties. A weight value of 10 was applied to the detection of the melting.

To decide on the "best" interatomic potential parametrization after the optimization, we selected the subset of all the sets of parameters predicting the melting in the estimated temperature range and defined a global objective function (GOF) combining the various loss functions:

$$\mathrm{GOF} = \sum_{i=1}^{i=N} \frac{\delta_i^r}{\sigma\left(\delta_i^r\right)} \quad (3)$$

Table 2 Fitting database for the reoptimization of Am^{4+} related terms

Property	Reference value	Tolerance
300 K lattice parameter (Å)	5.375[67]	0.05
300 K bulk modulus (GPa)	205[68]	50
Melting temperature (K)	Range: 3100–3400	Must be in the interval
1000 K lattice parameter (Å)	5.414[67]	No check
1000 K enthalpy increment (kJ mol^{-1})	55.8[69]	No check

with N the number of loss functions, δ_i^r the absolute relative error of the loss function i, and $\sigma(\delta_i^r)$ the standard deviation of δ_i^r over all sets of parameters evaluated during the optimization. This form allows one to add loss functions with various dimensions and to take into account their variability during the optimization. We finally selected the potential parametrization with the lowest GOF.

As for the optimization of the Am^{3+} and U^{5+} terms,[38] simulations for the optimization of the interatomic potential coefficients were carried out on 2592-atom supercells with a time step of 2 fs. The T_{damp} and P_{damp} parameters of the Nosé–Hoover thermostat and barostat were fixed at 0.1 ps and 0.5 ps, respectively. For simulations at room temperature, the cells are equilibrated for 8 ps and the properties are averaged over the last 4 ps. For higher temperature properties, the equilibration time was set at 10 ps, with properties averaged over the last 4 ps. The room-temperature bulk modulus was determined by applying ±4% deformations on the supercell equilibrated at 300 K. The relatively high-cost of a moving interface calculation is incompatible with the iterative scheme of the parameters optimization. The alternative is to equilibrate the supercell at two temperatures corresponding to the lower and upper bounds of our acceptable interval multiplied by an overestimation coefficient calibrated on previous HUM and MI calculations. We found this coefficient to be extremely consistent over the melting temperatures calculated on low-concentration uranium–americium mixed oxides,[38] with a value of 1.205 ± 0.005. We thus performed the two 30 ps equilibrations at 3100 K and 3400 K corresponding to corrected values of 2575 K and 2825 K, respectively. The interval was slightly broadened compared to the values determined in Section III.A to account for the uncertainties intrinsic to this method. We used the existence of the farthest peaks of the radial distribution functions or lack thereof to deduce the phase of the supercell. By ensuring that AmO_2 was solid at the lower bound of the range and liquid at its upper bound, we successfully incorporated the melting temperature in the optimization procedure.

III.C. Final set of parameters

The final Am^{4+}–O pair parameters as well as terms used for the other species are given in Table 3, while Table 4 regroups all the N-body terms with the updated values for Am^{4+}.

III.D. Validation of the updated interaction terms

III.D.1. Validation on AmO_{2-x}. We first applied the new terms on a HUM simulation, as well as elastic constants calculations, on stoichiometric AmO_2 to ensure that the potential is stable across the whole range of temperatures studied. Fig. 3 shows the comparison between the initial CRG potential, the new terms and the available data for the lattice parameter,[58,67] enthalpy increment[69] and bulk modulus[64,68,70,71] as a function of temperature. The available 0 K DFT+U calculated values are plotted at T = 300 K in the bulk modulus figure. The 141.5 GPa DFT+U value by Lu *et al.*[72] was disregarded here due to its large deviation with other studies, probably due to convergence issues in the DFT+U calculations.[70] Experimental data regarding the lattice parameter is truncated above 1073 K as the calculated O/M ratio deviates rapidly from 2.00 above this temperature.[17,58,59] We observe that the evolution with temperature of the structural, energetic and elastic properties indicates a physical behaviour of both sets of parameters.

We see that both the initial and new parametrizations are in excellent agreement with the available experimental data. They begin to behave differently above 2000 K and exhibit different melting temperatures, which can be identified by the

Table 3 Pair interaction terms of the potential, in bold the terms reoptimized in this study

Species α	Species β	$A_{\alpha\beta}$ (eV)	$\rho_{\alpha\beta}$ (Å)	$C_{\alpha\beta}$ (eV Å^6)	$D_{\alpha\beta}$ (eV)	$\gamma_{\alpha\beta}$ (Å^{-1})	$r^0_{\alpha\beta}$ (Å)
U^{4+}	U^{4+}	18600	0.2747	0.0			
U^{4+}	O^{2-}	448.779	0.387758	0.0	0.6608	2.05815	2.38051
U^{4+}	Am^{4+}	18600	0.2677	0.0			
Am^{4+}	Am^{4+}	18600	0.2609	0.0			
Am^{4+}	**O^{2-}**	**361.3445**	**0.41441**	0.0	**0.85916**	**2.01777**	**2.31482**
O^{2-}	O^{2-}	830.283	0.352856	3.884372			
Am^{3+}	U^{4+}	18600	0.248879	0.0			
Am^{3+}	U^{5+}	18600	0.234726	0.0			
Am^{3+}	Am^{3+}	18600	0.286433	0.0			
Am^{3+}	Am^{4+}	18600	0.272028	0.0			
Am^{3+}	O^{2-}	367.4422	0.381697	0.0	0.80836	2.16288	2.325338
U^{5+}	U^{4+}	18600	0.297631	0.0			
U^{5+}	U^{5+}	18600	0.256063	0.0			
U^{5+}	Am^{4+}	18600	0.286782	0.0			
U^{5+}	O^2	1157.0704	0.357723	0.0	1.85097	1.917152	1.916728

Table 4 N-Body interaction terms of the potential, in bold the terms reoptimized in this study

Species	G (eV Å$^{1.5}$)	η (Å^5)
U^{4+}	1.806	3450.995
U^{5+}	1.7921	3448.0359
Am^{3+}	0.3553	1630.7277
Am^{4+}	**1.3726**	**6034.3348**
O^{2-}	0.690	106.856

discontinuity in the enthalpy increment. As expected, the new terms yield a much lower melting point. To confirm this, we used the moving interface method with fifteen different seeds for the initialization of the velocities and found the new melting point to be (2792 ± 5.7) K. This is slightly higher than the upper bound of the interval determined in Section III.A and in excellent agreement with the estimate by Kato *et al.*[40]

III.D.2. Validation on (U,Am)O_2. Fig. 4 shows the evolution of the lattice parameter and the enthalpy increment as a function of temperature for $U_{0.3}Am_{0.7}O_2$ predicted by the original CRG and the updated parametrization, as well as the experimental data measured by Epifano *et al.*[17,19] The small discrepancy observed between the experimental and calculated lattice parameter (0.015 Å at 300 K) is due to the slight mismatch between the value of Epifano *et al.*[59] and that of Lebreton *et al.*,[16] which was included in the fitting database for the Am^{3+} and U^{5+} terms, as well as to the small difference in the Am content between the molecular dynamics simulations and the experiments (70% against 67%). Regarding the enthalpy increment, the values measured in ref. 17 showed a rather large deviation from the Neumann–Kopp law, which the authors explained by a probable reduction of the sample. This excess enthalpy at high temperature in the experimental data accounts for part of the difference with the calculated values for a perfectly stoichiometric compound. As expected given the small differences previously observed on AmO_2 for $T < 1500$ K, there is little to no change between both parametrizations. The evolution of energetic and structural properties with temperature is reproduced well by both sets of parameters.

As a final validation, we investigate the difference between both parametrizations on the 0 K enthalpy of mixing, shown in Fig. 5. The enthalpy of mixing of uranium–americium mixed oxides is defined as:

$$\Delta H_{\mathrm{mix}} = H^{\mathrm{U_{1-y}Am_yO_2}} - (1-y)H^{\mathrm{UO_2}} - yH^{\mathrm{AmO_2}} \qquad (4)$$

It can be observed that only the interatomic potentials including the Am^{3+} and U^{5+} oxidation states yield negative values for the mixing enthalpy – indicative of a stable solid solution – also calculated in DFT+U,[45] as values calculated with two potentials taking into account only the (+IV) oxidation states yield unphysical positive values.[73] Moreover, the values obtained with the new parametrization are in much better agreement with the DFT+U-calculated ones due to the change in the absolute value of AmO_2 enthalpy content. The results are also in good agreement with the calculated values at 300 K with the CALPHAD model.[74] Since the enthalpy of mixing was not included in the fitting procedure, this is an important result for the validation of the reoptimized parameters.

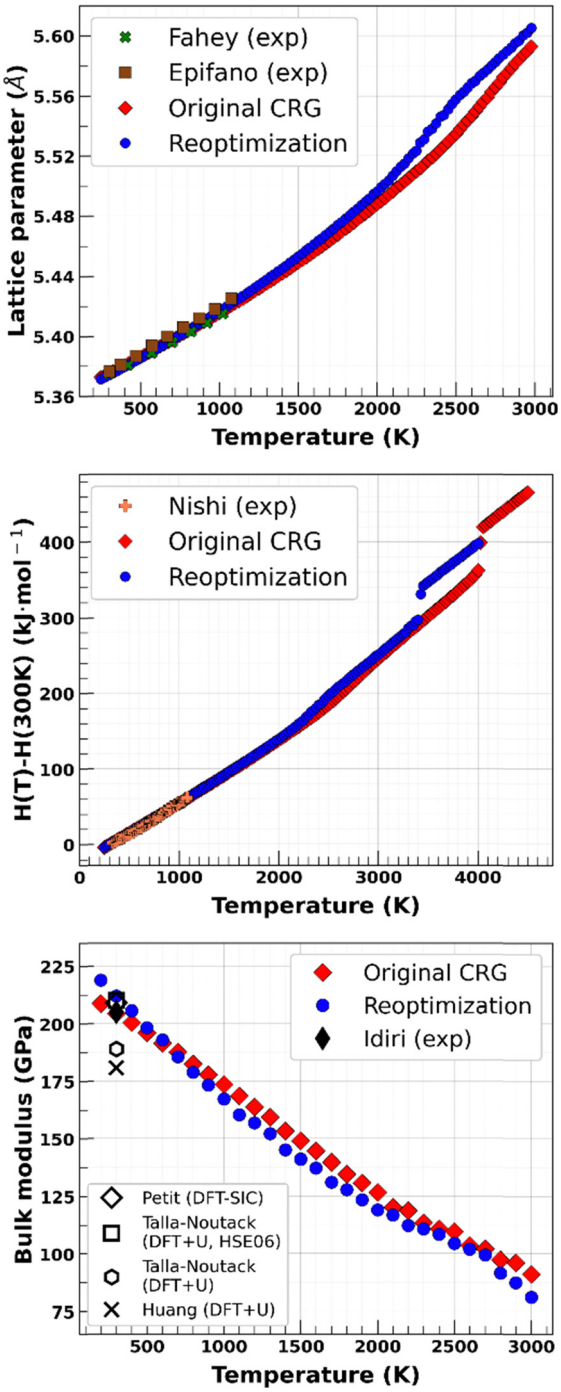

Fig. 3 Comparison of properties yielded by both sets of parameters and available experimental data for the lattice parameter[58,67] (top), the enthalpy increment[69] (middle) and the bulk modulus[64,68,70,71] (bottom) as a function of temperature.

IV. Results and discussion

We apply our parametrization to the calculation of properties of interest of (U,Am)O_{2-x} oxides. We present here the results, separating the properties directly obtained as a function of temperature during HUM calculations, their derivative properties,

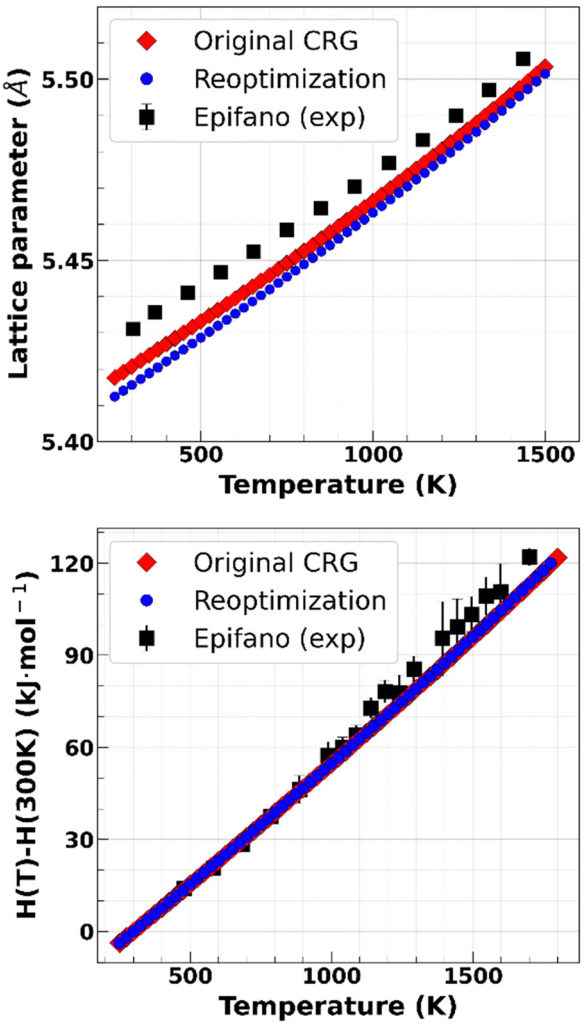

Fig. 4 Comparison of properties yielded by both sets of parameters and available experimental data for the lattice parameter[19] (top) and the enthalpy increment[17] (bottom) as a function of temperature for $U_{0.3}Am_{0.7}O_2$.

the melting temperature estimates yielded by the MI method and the elastic properties.

IV.A. Direct properties

IV.A.1. Structural properties. The calculated room-temperature lattice parameter is shown in Fig. 6 for $U_{1-y}Am_yO_{2-x}$ with $0 \leq y \leq 1$ and $0 \leq x \leq 0.1$ and compared to experimental data measured by Lebreton *et al.*[16] and DFT+*U* calculations performed by Talla-Noutack *et al.*,[45] whose results were rescaled to match the experimental lattice parameter of pure oxides. The results for Am contents up to 50% and with O/M = 2.00 are taken from our previous study.[38] The lattice parameter increases when the O/M ratio decreases, which is common in oxides.[75] The magnitude of this expansion depends on the americium content. Medium concentrations are less impacted, leading to a quasi-linear room-temperature lattice parameter for $(U,Am)O_{1.90}$ compounds. $U_{0.5}Am_{0.5}O_{2-x}$ compositions have a peculiar behaviour, the lattice-parameter remaining quasi-constant and even decreasing slightly for some O/M ratios. This is probably due to the larger uncertainty

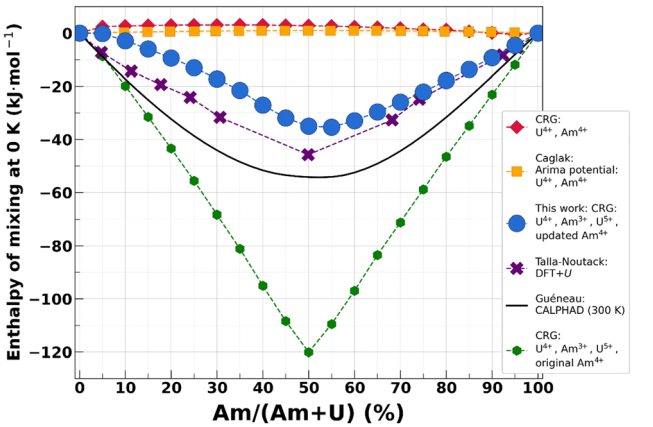

Fig. 5 Comparison of the 0 K enthalpy of mixing computed using the original CRG potential (red diamonds), the Arima potential[73] (yellow squares), the CRG potential augmented with Am^{3+} and U^{5+} oxidation states (green hexagons),[38] the CRG potential with Am^{3+}; U^{5+} and reoptimized Am^{4+} parameters (blue circles, this work), DFT+*U*[45] (purple crosses) and CALPHAD[74] (black line).

(not shown here for clarity) in the calculation of structural properties observed at lower temperature for this americium content, as discussed in ref. 38.

Fig. 7 shows the evolution of the lattice parameter and density as a function of temperature for stoichiometric uranium–americium mixed oxides. We can clearly see a change in the trend of the evolution of structural properties as a function of americium content occurring at an Am content of 50%: the lattice parameter (resp. the density) remains relatively similar from UO_2 to $U_{0.5}Am_{0.5}O_2$ while decreasing (resp. increasing) rapidly between 50% Am and AmO_2. This is due to the change in the cationic oxidation states taking place at 50% Am, shown in Fig. 1, which impact the interatomic distances.[38] At higher temperature, the two properties show a subtle inflection point with a temperature dependence on the americium content. This is associated with the Bredig transition predicted by the interatomic potential in these

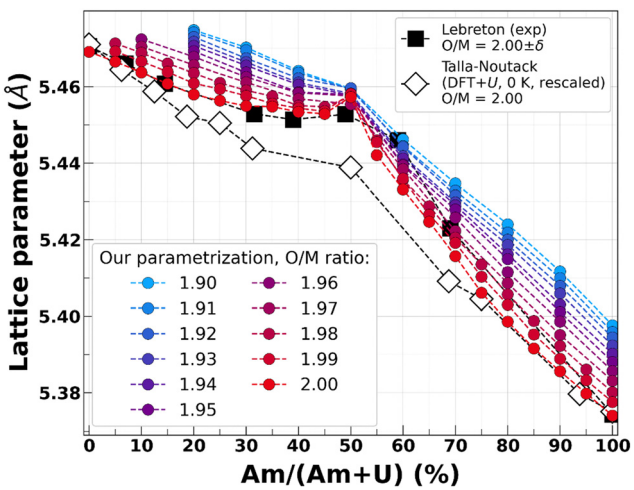

Fig. 6 Room-temperature lattice parameter of $(U,Am)O_{2-x}$ compounds, including data of ref. 38, compared to experimental data measured by Lebreton[16] and DFT+*U* calculations performed by Talla-Noutack.[45]

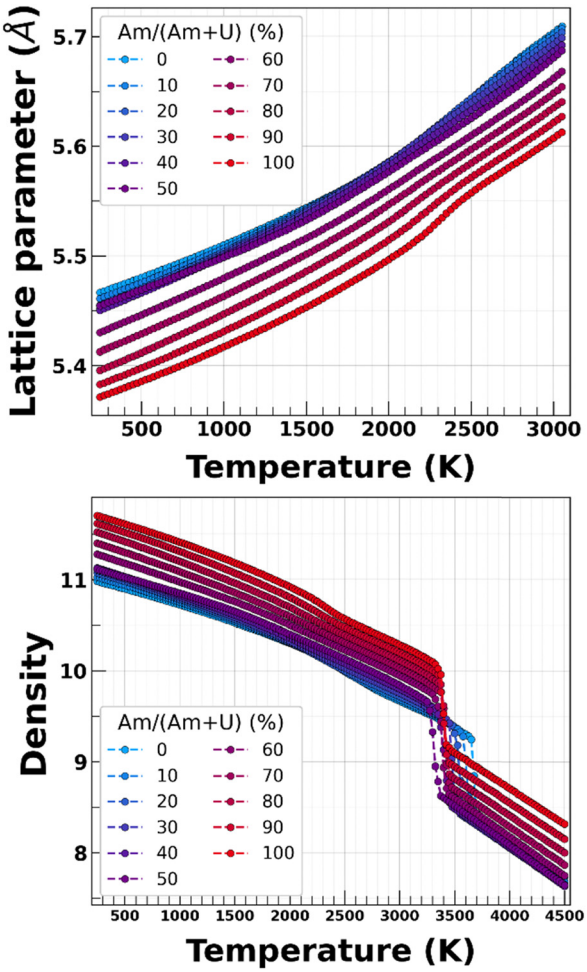

Fig. 7 Evolution of the lattice parameter (top) and density (bottom) as a function of temperature for stoichiometric uranium–americium mixed oxides, including data of ref. 38.

compounds. This transition is discussed in more detail in Section IV.B relative to the derivative properties.

Then, around 3300–3600 K, the discontinuity in the density increment curves indicates the melting. Although the melting temperature T_m is overestimated by this simulation technique, it can already be seen that the melting temperature is very similar for all Am contents between 50% and 100% and that it is between the melting temperature of $U_{0.5}Am_{0.5}O_2$ and that of UO_2. Melting temperatures are discussed extensively in Section IV.C, which describes the results of the moving interface method.

The effect of the oxygen to metal ratio on the lattice parameter as a function of temperature is shown in Fig. 8 for three Am contents (20%, 50% and 80% Am). The same trend is observed in the variation of the cell parameter with the O/M ratio for the three Am contents: an increase up to approximately 1900 K and a decrease above this temperature. Quantitatively, however, these changes depend significantly on the americium content. Low americium contents are impacted both at low and high temperature; medium americium contents are virtually unaffected by the O/M ratio and high Am-contents are affected only at low temperature. We can also see O/M-dependent

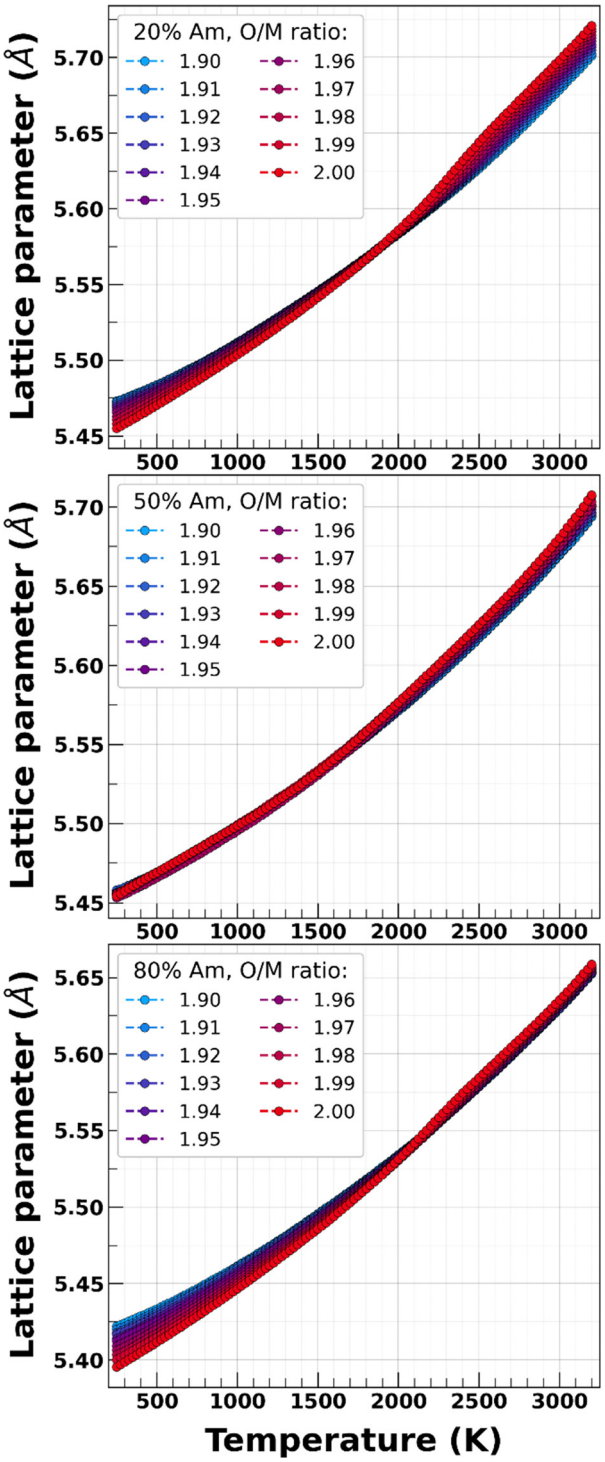

Fig. 8 Lattice parameter as a function of temperature for $U_{0.8}Am_{0.2}O_{2-x}$ (top), $U_{0.5}Am_{0.5}O_{2-x}$ (middle) and $U_{0.2}Am_{0.8}O_{2-x}$ (bottom) for oxygen to metal ratios from 1.90 to 2.00.

changes in the inflexion point associated with the Bredig transition (see Section IV.B).

IV.A.2. Energetic properties. The enthalpy increment of stoichiometric (U,Am)O_2 is shown in Fig. 9 for several americium contents. No impact of the Am content is seen up to 2000 K. As with the lattice parameter and density, this property shows a

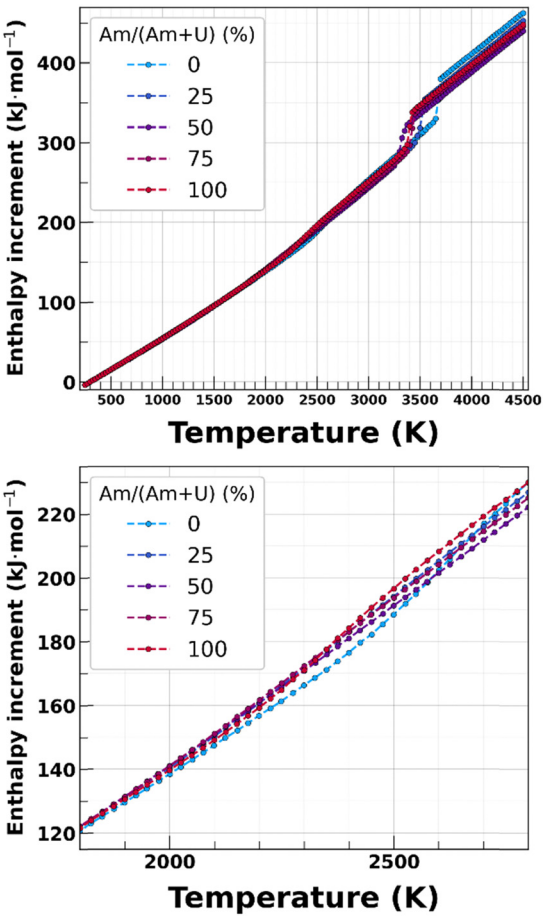

Fig. 9 Enthalpy increment as a function of temperature for stoichiometric uranium–americium mixed oxides (top, magnification on bottom), including data of ref. 38.

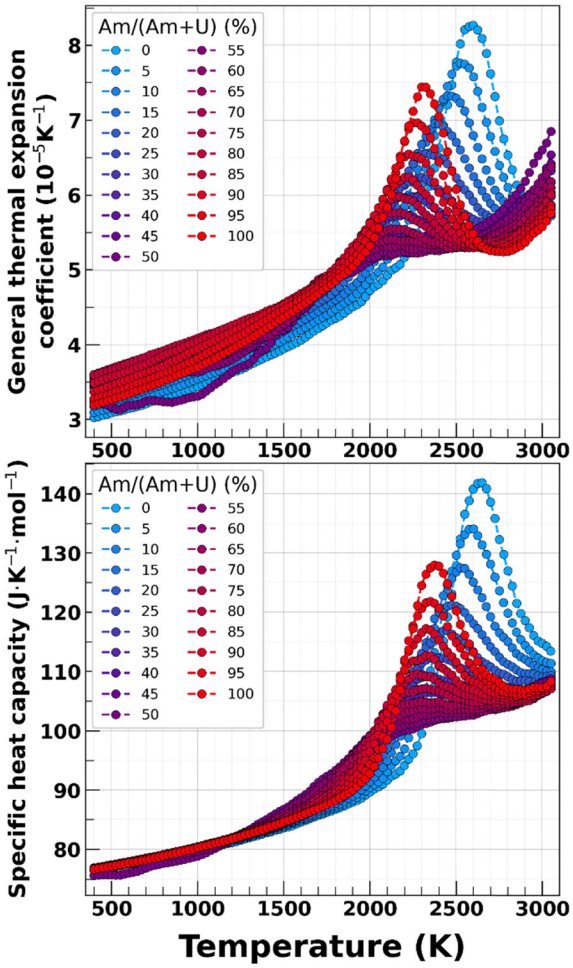

Fig. 10 General thermal expansion coefficient (top) and specific heat capacity (bottom) as a function of temperature for (U,Am)O_2 compounds. Values up to 50% Am/(Am + U) are taken from ref. 38.

subtle inflection point for which the temperature depends on the americium content, associated with the Bredig transition. The enthalpy of fusion $\Delta_{fus}H^\circ$ can be estimated approximately by fitting two linear functions to the high-temperature solid part and to the liquid part of the enthalpy increment. It is difficult, however, to assess precisely the temperatures at which the melting process begins and ends, in part due to the averaging of properties over different supercells and velocity seeds in which the melting temperature varies slightly. A conservative approach enables us to estimate an enthalpy of fusion in the 38 kJ mol^{-1} to 52 kJ mol^{-1} range for all americium contents, without a clear evolution trend with the Am content. There is no experimental value for AmO_2: the only two measurements of enthalpy of fusion of actinide dioxides are for UO_2, with values of 74 kJ mol^{-1} by Hein and Flagella[76] and 76 kJ mol^{-1} by Leibowitz *et al.*[77] In addition, the enthalpy of fusion of PuO_2 was estimated to be (64 ± 6) kJ mol^{-1} by Konings *et al.*[62] using enthalpy measurements performed by Ogard[78] in combination with the entropy of fusion of UO_2.

The impact of the oxygen to metal ratio on the enthalpy per atom is similar for all temperatures and compositions: the larger the deviation from O/M = 2.00 in the hypostoichiometric domain, the higher the enthalpy, as shown in Appendix A (Section A.1) for three Am/(Am + U). This is consistent with the enthalpy values calculated using the CALPHAD method in (U,Pu)O_{2-x} by Fouquet-Métivier *et al.*[79]

IV.B. Derivative properties

The general thermal expansion coefficient α and specific heat capacity c_p are defined as:

$$\alpha = \frac{1}{V}\left(\frac{\partial V}{\partial T}\right)_P \quad (5)$$

$$c_p = \left(\frac{\partial H}{\partial T}\right)_P \quad (6)$$

From the values of the lattice parameter and enthalpy increment calculated as a function of temperature, we computed these two derivatives using the finite difference method:

$$\left(\frac{\partial X}{\partial T}\right)_P = \frac{X_{T-\frac{\Delta T}{2}} - X_{T+\frac{\Delta T}{2}}}{\Delta T} \quad (7)$$

We included the three neighbouring values (±25 K, 50 K and 75 K) in the derivation to slightly refine the derivatives.

The evolution of α and c_p with respect to temperature is shown in Fig. 10 for stoichiometric (U,Am)O_2 compounds.

We consider both properties concurrently due to their nearly identical evolution as a function of temperature, focussing on americium contents above 50%. Their evolution with temperature is qualitatively identical to that of low americium contents mixed oxides:[38] first a regular rise up to 1700 K, followed by a peak. The influence of the Am content up to 1700 K is more pronounced for the general thermal expansion coefficient than for the specific heat capacity. Medium americium contents have a generally higher thermal expansion coefficient than the pure oxides in this temperature region. The comparison of the specific heat capacity calculated with the values derived from enthalpy measurements performed by Epifano *et al.*[17] is not conclusive due to the slight but systematic underestimation of this property by the CRG formalism, as well as to the possible changes in the experimental O/M ratio affecting the measurements.

The peaks observed in the derivative properties are related to the Bredig transition,[80] observed in many compounds with fluorite structure including UO_2.[81–85] It is also predicted by atomic scale calculations using various interatomic potentials for UO_2,[24,86–88] including machine-learning potentials trained on DFT+U data,[89] using the CRG potential for PuO_2 and using *ab initio* molecular dynamics in UO_2 and PuO_2.[90] The CRG potential also predicts this transition in (U,Pu)O_2,[25,32,35] (U,Th)O_2,[26] (U,Am)O_2[34] and (U,Gd)O_2.[29] The Bredig transition is commonly admitted to be a superionic transition with the temperature T_B of the maximum of the peak empirically considered to be approximately $T_B \approx 0.8 \times T_m$, but the origin of the oxygen diffusion acceleration is still a matter of debate. Several modelling[91–93] and experimental works[81,83,84] were dedicated to the clarification of the underlying mechanisms with no consensus reached to this day.

In the case of (U,Am)O_2 compounds, the amplitude and temperature of the peak are strongly dependent on the Am content. From UO_2 to $U_{0.5}Am_{0.5}O_2$, the temperature and amplitude of the peak decrease strongly and it becomes difficult to identify the peak for medium americium contents. For Am-rich compounds, the amplitude of the peak increases with the americium content while its temperature is relatively stable due to the low impact of the Am content on the melting temperature (see next section). The change in the trend of the evolution of the Bredig peak amplitude and temperature with americium content is a direct consequence of the change in the cationic oxidation states occurring at 50% Am, as seen in Fig. 1. The Bredig transition in pure americium dioxide is not a feature of the reoptimized Am^{4+} potential terms, it was yielded by the original CRG terms with the same amplitude at a higher temperature (2800 K).[34] It is noteworthy that both parametrizations yield this behaviour, as it confirms that the only difference between the two sets of parameters is the melting temperature.

We also studied the effect of the O/M ratio on the derivative properties. Fig. 11 presents the general thermal expansion coefficient for all O/M ratios studied for two mixed oxides, as well as for AmO_{2-x}. The effect of an increasing deviation from O/M = 2.00 on α is twofold. First, for temperatures below 1700 K, it results in a decreasing general thermal expansion coefficient. The intensity of this decrease depends on the americium content. Second, the Bredig peak is shifted at higher temperature, while its amplitude decreases. While all compositions seem to be affected qualitatively in the same manner, the temperature and amplitude of the peak also depends on the americium content, the peak disappearing

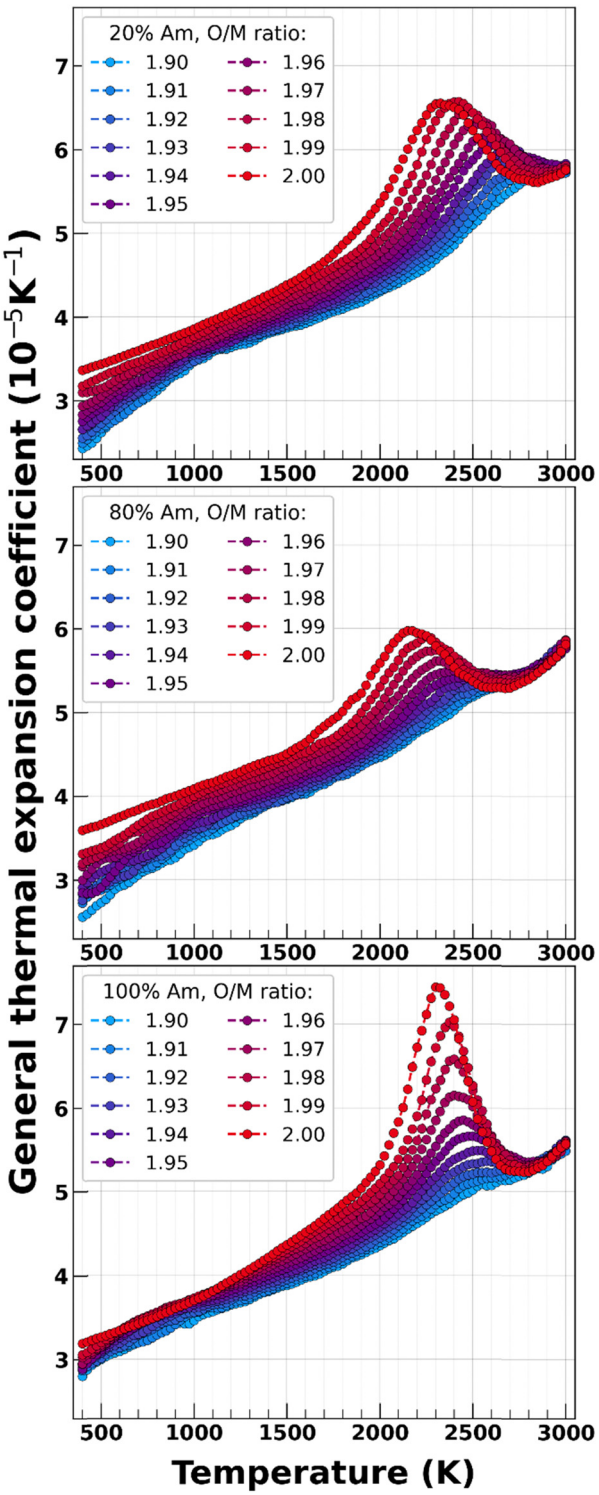

Fig. 11 General thermal expansion coefficient as a function of temperature for $U_{0.8}Am_{0.2}O_{2-x}$ (top), $U_{0.2}Am_{0.8}O_{2-x}$ (middle) and AmO_{2-x} (bottom) for oxygen to metal ratios from 1.90 to 2.00.

entirely for $AmO_{1.90}$. The fact that the Bredig peak disappears for low O/M ratios, which is also the case in the empirical potential calculations of $(U,Pu)O_{2-x}$,[94] could explain why this transition has not been observed yet in $(U,Pu)O_2$ and $(U,Am)O_2$ mixed oxides.

The evolution of the specific heat capacity as a function of temperature is shown in Fig. 12 for the same compositions. The effect of the O/M ratio on c_p is different from what is observed for the thermal expansion α. The simulations show no impact of the O/M ratio on the specific heat capacity values up to the onset of the peak. When O/M decreases, the peak is shifted towards higher temperatures for all Am contents. This is in line with the experiments performed on UO_2 by J. P. Hiernaut *et al.*,[83] which showed that successive shots – associated to a reduction of the sample – yielded higher temperatures for the Bredig transition. The amplitude of the peak, however, evolves differently for the three Am contents. For 20% Am, the amplitude is virtually unchanged, as the difference between the c_p values at the maxima corresponds to the difference between the c_p values at the onset of the transition. For 80% Am, the peak decreases while flattening rapidly into a plateau. Finally, for AmO_{2-x}, the decrease is more pronounced and the peak transforms into a plateau only at lower O/M values around 1.93.

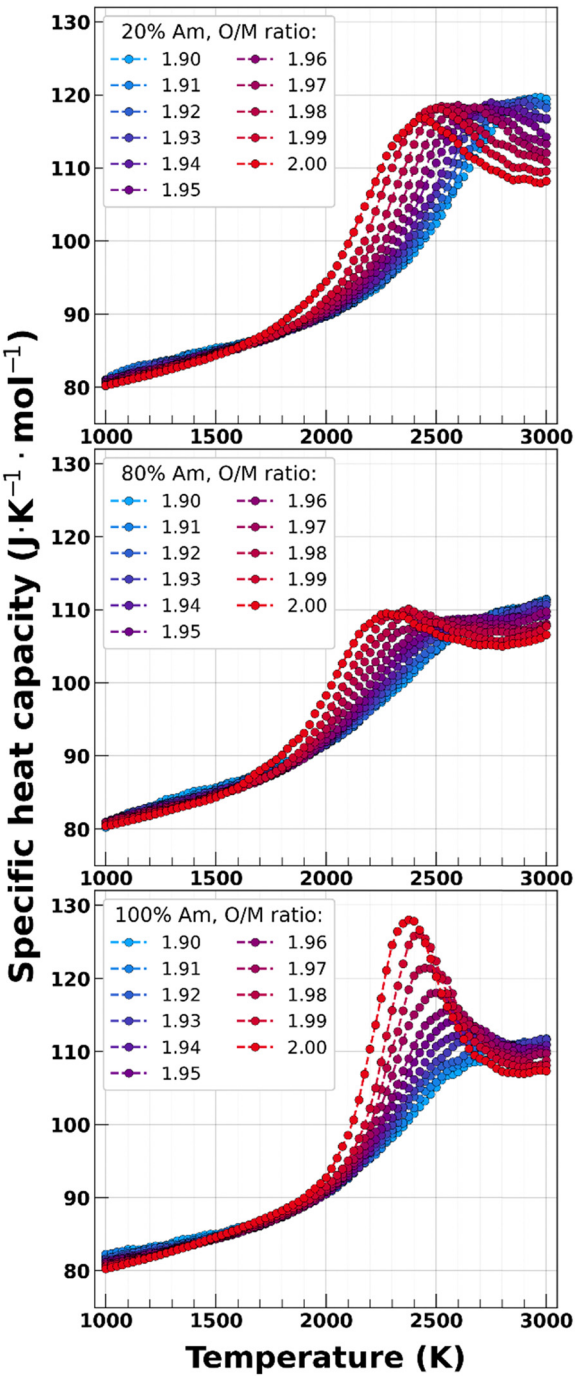

Fig. 12 Specific heat capacity as a function of temperature for $U_{0.8}Am_{0.2}O_{2-x}$ (top), $U_{0.2}Am_{0.8}O_{2-x}$ (middle) and AmO_{2-x} (bottom) for oxygen to metal ratios from 1.90 to 2.00.

Based on our calculations as well as on the results of empirical potential calculations conducted on $(U,Pu)O_{2-x}$[94] and $(U,Pu,Gd)O_{2-x}$[29] using the same potential formalism, the conclusion as follows can be drawn concerning the evolution of the specific heat capacity with composition:

- As seen in AmO_{2-x}, $U_{1-y}Am_yO_{2-x}$ with $y > 0.5$, $(U,Pu)O_{2-x}$ and $(U,Pu,Gd)O_{2-x}$, the inclusion of oxygen vacancies associated with cations in the (+III) oxidation state results in a significant decrease of the Bredig peak amplitude, while increasing slightly its temperature.
- From the results on $(U,Am)O_2$ and $(U,Pu,Gd)O_2$ compounds, the inclusion of (+III) cations associated to (+V) ones while keeping O/M = 2.00 (without O vacancies) results in a decrease of both the amplitude and temperature of the Bredig transition.
- Compounds with a cationic sublattice composed of (+V) and (+III) cations in equal proportions, such as $U_{0.5}Am_{0.5}O_2$, do not seem to exhibit a Bredig transition.
- Finally, as seen in $U_{1-y}Am_yO_{2-x}$ with $y < 0.5$, the inclusion of oxygen vacancies accommodated by the reduction of a (+V) cation to (+IV) results in a shift of the Bredig peak towards higher temperatures while leaving its amplitude unchanged.

From these we infer that, using the CRG formalism:

- The presence of (+III) cations tends to lower the amplitude of the Bredig peak.
- The presence of (+III) and/or (+V) cations tend to lower the Bredig peak temperature.
- Oxygen vacancies tend to increase the Bredig peak temperature.

Since we cannot perform simulations separating the effect of oxygen vacancies from that of changes in the oxidation states due to the charge neutrality of the supercells in our simulations, some of these effects could be coupled and/or could cancel each other out.

IV.C. Melting temperature estimates

Fig. 13 compares the estimates of the melting temperature for each composition yielded by the original Am^{4+} parameters and the reoptimized terms. The results for compounds with less than 50% Am are unaffected by Am^{4+} parameters since this oxidation state is not present for these compositions. The slope discontinuity exhibited by both parametrizations is once again due to the change in oxidation state at Am/(Am + U) = 0.5 (see Fig. 1). We observe a very large difference between the two sets of parameters on T_m for Am-rich compositions, our parametrization yielding much lower melting temperatures. For AmO_2, the new value is (2792 ± 5.7) K,

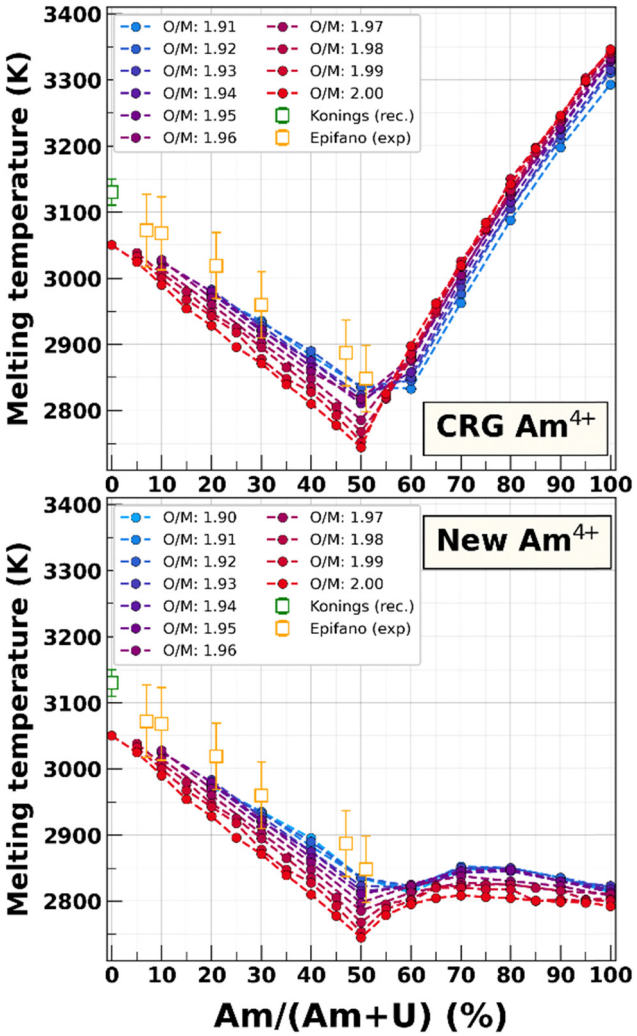

Fig. 13 Estimates of the melting temperatures of $U_{1-y}Am_yO_{2-x}$ using the original CRG Am^{4+} parameters (top) and the set of terms obtained in this work (bottom). Available experimental data[20,62] is shown as empty squares for comparison.

as opposed to (3346 ± 5.7) K with the original CRG potential. We can also see that the melting temperature of Am-rich compositions yielded by our parameters varies only slightly with Am content, with a possible local maximum reached for compositions around 70% Am for all studied O/M ratio. An important observation is that the melting temperature is close to the linear interpolation between UO_2 and $U_{0.5}Am_{0.5}O_2$ for Am contents lower than 50% and between $U_{0.5}Am_{0.5}O_2$ $U_{0.5}$ and AmO_2 for higher contents. The confirmation of the melting temperatures for $(U,Am)O_2$ with high Am contents could thus enable one to obtain a better estimate for the melting temperature of AmO_2.

The difference in the effect of the O/M ratio between the two parametrizations should also be noted. Using the original Am^{4+} parameters, the deviation from O/M = 2.00 had opposing effects on the melting temperature for low and high Am contents, increasing T_m for Am/(Am + U) $\leq$ 50% while decreasing it for Am-rich compositions. In contrast, the reoptimized potential predicts that a decrease in the O/M ratio increases the melting temperature for all Am contents, which is consistent with the shift of the Bredig transition temperature (see Section IV.B). This is in line with the results of the CALPHAD calculations using the TAF-ID database, which predict the congruent melting to be in the hypostoichiometric region for all Am contents in uranium–americium mixed oxides.[74] This is also similar to the solid/liquid phase transition in MOX calculated using the CALPHAD method by Fouquet-Métivier *et al.*[79] They proposed a stabilising mechanism due to an increase in the entropy that lowers the Gibbs free energy of the system and thus increases T_m for hypostoichiometric domains for all plutonium contents. They show that this entropy increase is due to the presence of plutonium in a mixed Pu^{4+}/Pu^{3+} oxidation state to accommodate the oxygen vacancies in the hypostoichiometric compositions. Given the similarity in the oxidation states of plutonium and americium in actinide oxides, this explanation could also be valid for the U–Am–O system.

IV.D. Elastic properties

There is no measurement or first-principle calculation of the elastic properties of uranium–americium mixed oxides, these are therefore first estimates. The evolution with temperature of C_{11}, C_{12}, C_{44} and the Zener ratio for stoichiometric $(U,Am)O_2$ compounds is shown in Fig. 14. The plots representing several isotherms of the elastic constants for $(U,Am)O_2$ compounds can be found in Appendix B (Section B.1.1).

Elastic constants tend to decrease with temperature, indicating a softening of the materials. C_{12} exhibits a non-monotonous evolution with temperature: its value increases between 2300 K and 2800 K for UO_2 and AmO_2 as well as for low and high Am contents, in line with measurements by Hutchings on UO_2,[81] while it decreases steadily for $U_{0.5}Am_{0.5}O_2$ from 300 K to 3000 K. We therefore infer that this increase is a direct consequence of the Bredig transition.

For all Am contents, the Zener ratio is low at room temperature, showing a significant anisotropy of the $(U,Am)O_2$ compounds. It is higher for medium Am contents. For low and high Am contents, the Zener ratio remains relatively constant up to approximately to 2000 K, *i.e.*, until the onset of the Bredig transition, due to the concomitant decrease of C_{11}, C_{12} and C_{44}. Above 2000 K, the Bredig transition affects the elastic constants in different ways, leading to a strong increase of the Zener ratio with temperature, which indicates a significant increase in the material isotropy. Medium compositions, in particular $U_{0.5}Am_{0.5}O_2$, exhibit a rather steady evolution of all three independent elastic constants with temperature but with different temperature dependences, leading to a more progressive increase of the Zener ratio.

The variation of the elastic constants and Zener ratio as a function of the O/M ratio is similar for all Am contents. Fig. 15 shows the variation of the elastic constants and of the Zener ratio of $U_{0.8}Am_{0.2}O_{2-x}$ with temperature for all O/M ratio studied as an example. Additional results for two other americium contents (50% and 80% Am) can be found in Appendix B (Section B.1.2).

The modifications induced by the O/M ratio on the lattice parameter cause an opposite variation in C_{11}: the increase of

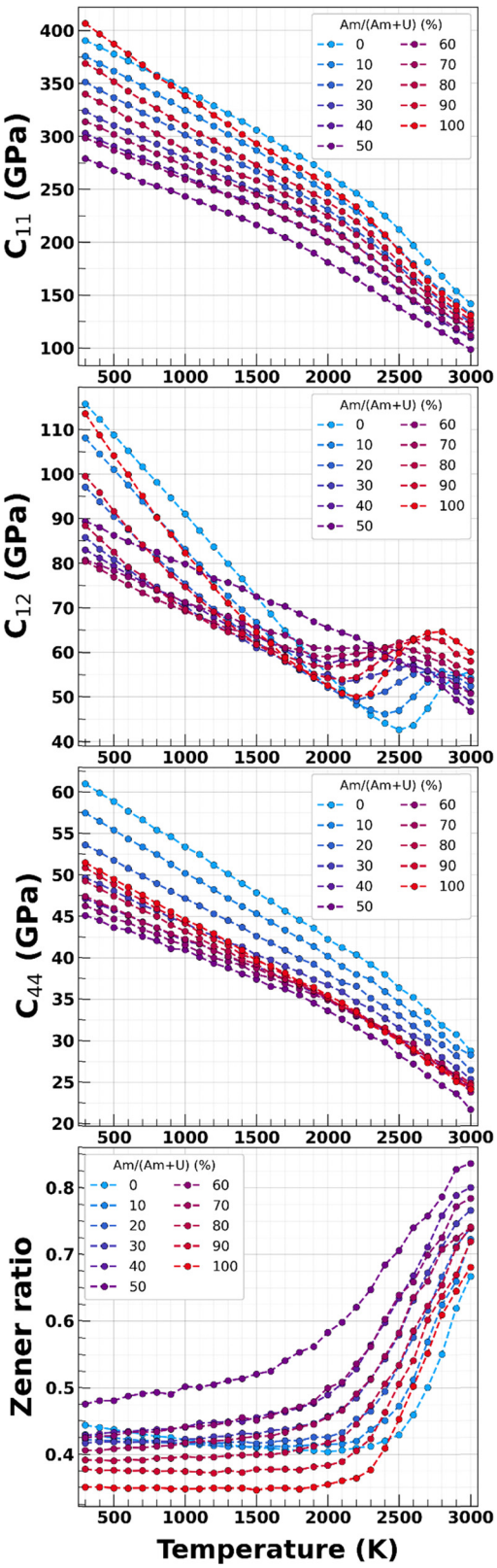

Fig. 14 Evolution with temperature of (a) C_{11} (b) C_{12} (c) C_{44} (d) the Zener ratio for $(U,Am)O_2$ compounds.

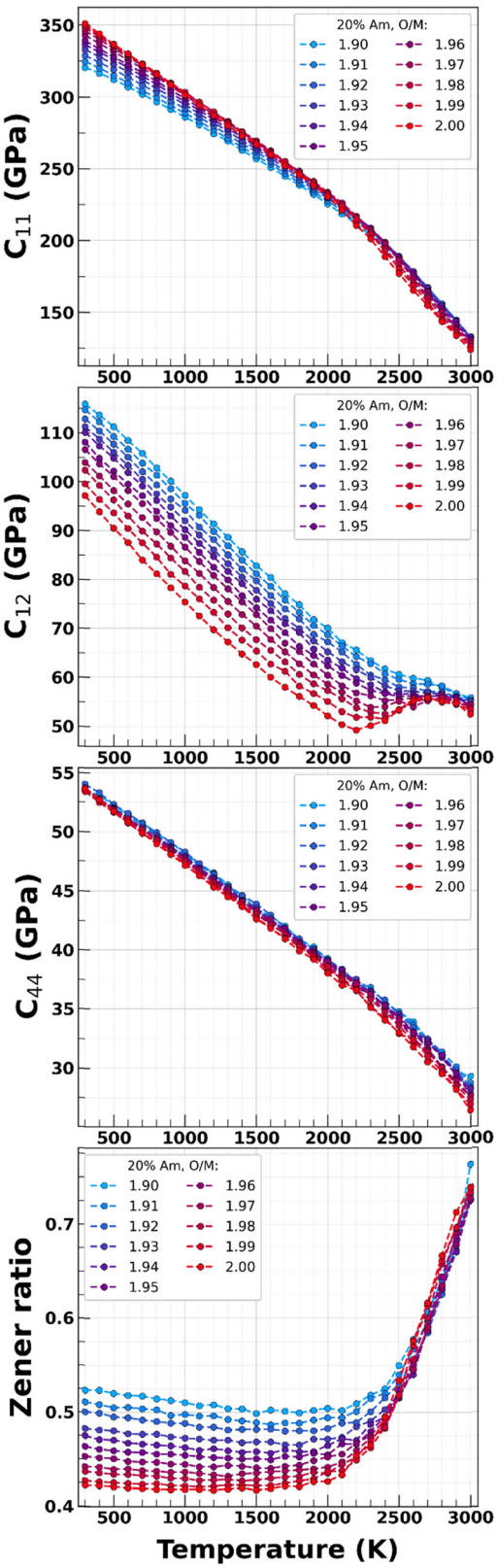

Fig. 15 Evolution with temperature of (a) C_{11} (b) C_{12} (c) C_{44} (d) the Zener ratio for $U_{0.8}Am_{0.2}O_{2-x}$ compounds with $0 \leq x \leq 0.1$.

the lattice parameter with decreasing oxygen content at low temperature induces a decrease in C_{11} and the opposite behaviour is observed at high temperature. The amplitude of the increase in C_{12} at high temperature can be correlated to the

intensity of the Bredig peak in the general thermal expansion coefficient (see Fig. 11). The effect of the oxygen content on C_{44}, indicative of the resistance to shear stress, is generally less significant but non negligible in particular for $U_{0.5}Am_{0.5}O_{2-x}$. Finally, the Zener ratio increases when O/M decreases for temperatures lower than 2000 K, but the effect of the hypostoichiometry becomes negligible at higher temperatures for which stoichiometric materials are already nearly isotropic.

It can be noted that the behaviour of the elastic properties with the O/M ratio observed for Am contents below 50% is similar to that obtained by Porto *et al.* in $(U,Pu)O_{2-x}$ using the CRG potential.[94] They took into account the same oxidation states as in $(U,Am)O_{2-x}$ for the cationic sublattice: U^{4+}, U^{5+}, and Pu^{3+} and Pu^{4+} instead of Am^{3+} and Am^{4+}.

V. Conclusion

We reoptimized the interactions terms involving Am^{4+} cations of the CRG potential to lower the calculated melting temperature of AmO_2 and used this parametrization in combination with U^{4+} parameters as well as previously optimized Am^{3+} and U^{5+} terms to perform a systematic study of the structural, thermodynamic and elastic properties of $U_{1-y}Am_yO_{2-x}$ with $0 \leq y \leq 1$ and $0 \leq x \leq 0.1$.

Significant differences are observed between Am contents less than and greater than 50%, which can be correlated to the changes in the cationic oxidation states present in these compounds. Of particular interest is the prediction by the potential of a Bredig transition for the majority of the studied compositions, including AmO_2, as well as for most hypostoichiometric compositions. The existence of a Bredig peak, however, is unclear for medium americium contents. In addition, the melting temperature is now more in line with basic thermodynamic data and the effect of the O/M ratio on this phase transition is consistent with CALPHAD predictions using the TAF-ID. Finally, elastic properties of $(U,Am)O_{2-x}$ compounds were evaluated for the first time.

These results will be useful for the CALPHAD modelling of Am-bearing oxides, as well as for the simulation of $(U,Am)O_2$ fuel pellet at the mesoscopic and macroscopic scale. Additional experimental characterizations and/or electronic structure calculations on selected compositions, however, would be needed to confirm these results, especially for high americium contents and at high temperature.

Data availability

Data are available in the Zenodo repository of the PATRICIA H2020 European project: **https://zenodo.org/communities/patricia/records?q=&l=list&p=1&s=10&sort=newest**.

Conflicts of interest

There are no conflicts to declare.

Appendices

Appendix A

A.1. Enthalpy variation with O/M ratio. Fig. 16 shows the variation of the enthalpy in $(U,Am)O_{2-x}$ as a function of the O/M ratio for three Am contents.

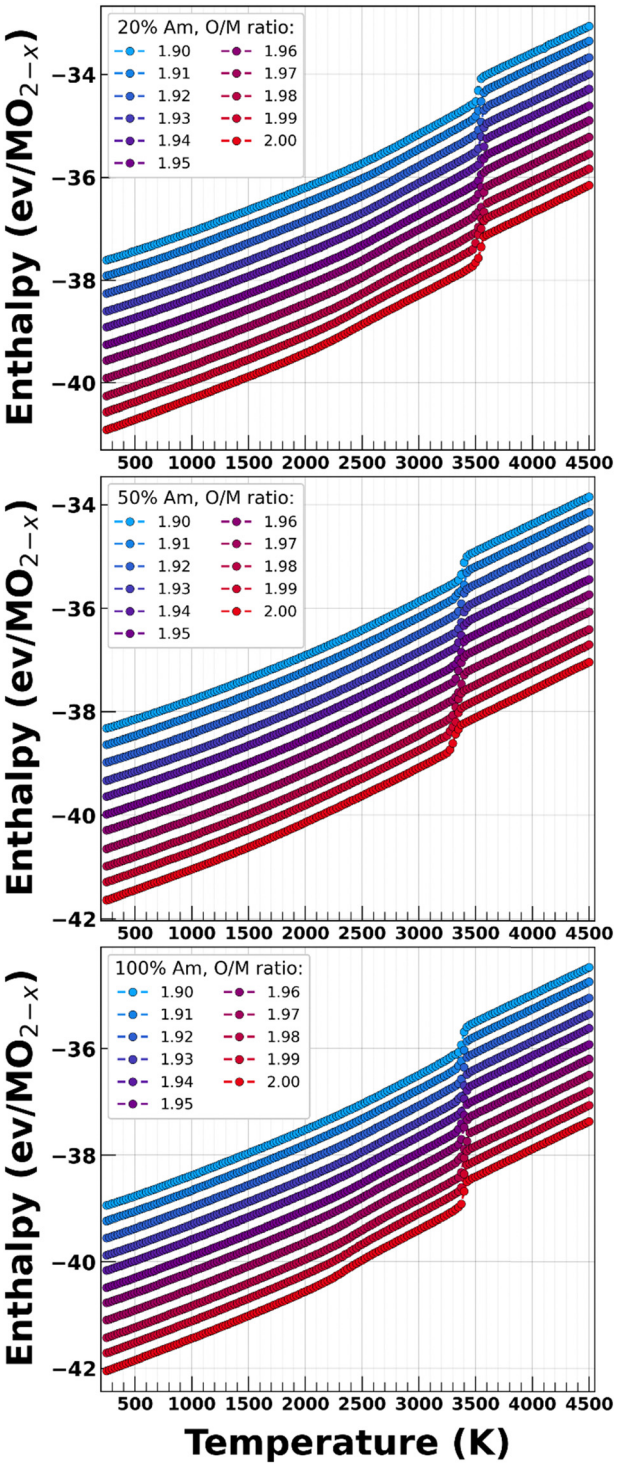

Fig. 16 Enthalpy as a function of temperature for uranium–americium mixed oxides including 20% Am (top), 50% Am (middle) and 100% Am (bottom).

Appendix B

B.1. Elastic properties

B.1.1. Isotherms. At low temperature, the elastic properties exhibit three types of evolution with the Am content, as shown in Fig. 17: a "V" (or "U") shape, a "W" shape, or a "Δ" shape. This is consistent with the fact that the cationic concentrations in these oxides are linearly dependent on the americium content for the two sections UO_2 to $U_{0.5}Am_{0.5}O_2$ and $U_{0.5}Am_{0.5}O_2$ to AmO_2 (see Fig. 1).

B.1.2. Effect of the O/M ratio on the elastic properties. Fig. 18 shows the effect of the O/M ratio on the evolution with temperature of C_{11}, C_{12}, C_{44} and the Zener ratio in $(U,Am)O_{2-x}$ for 2 Am contents.

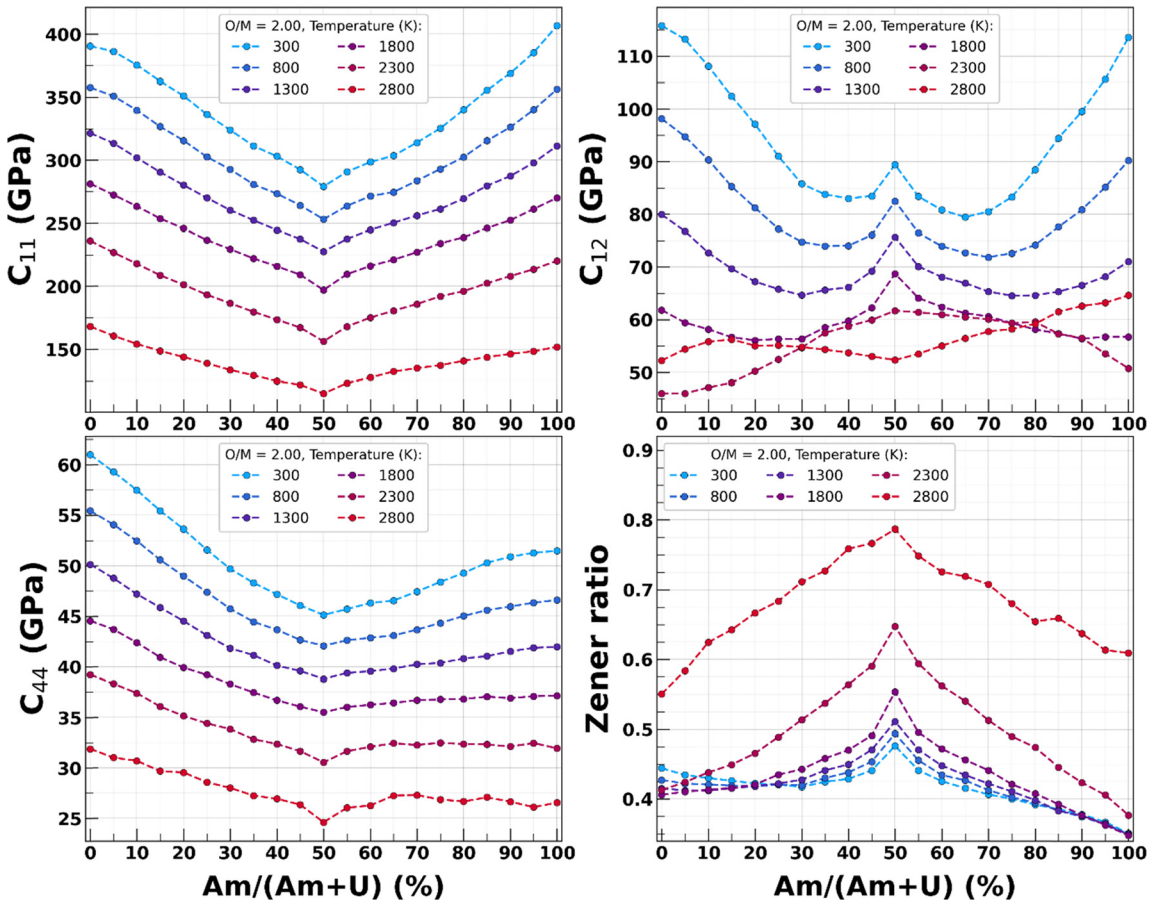

Fig. 17 Isotherms of (a) C_{11} (b) C_{12} (c) C_{44} (d) the Zener ratio for $(U,Am)O_2$ compounds.

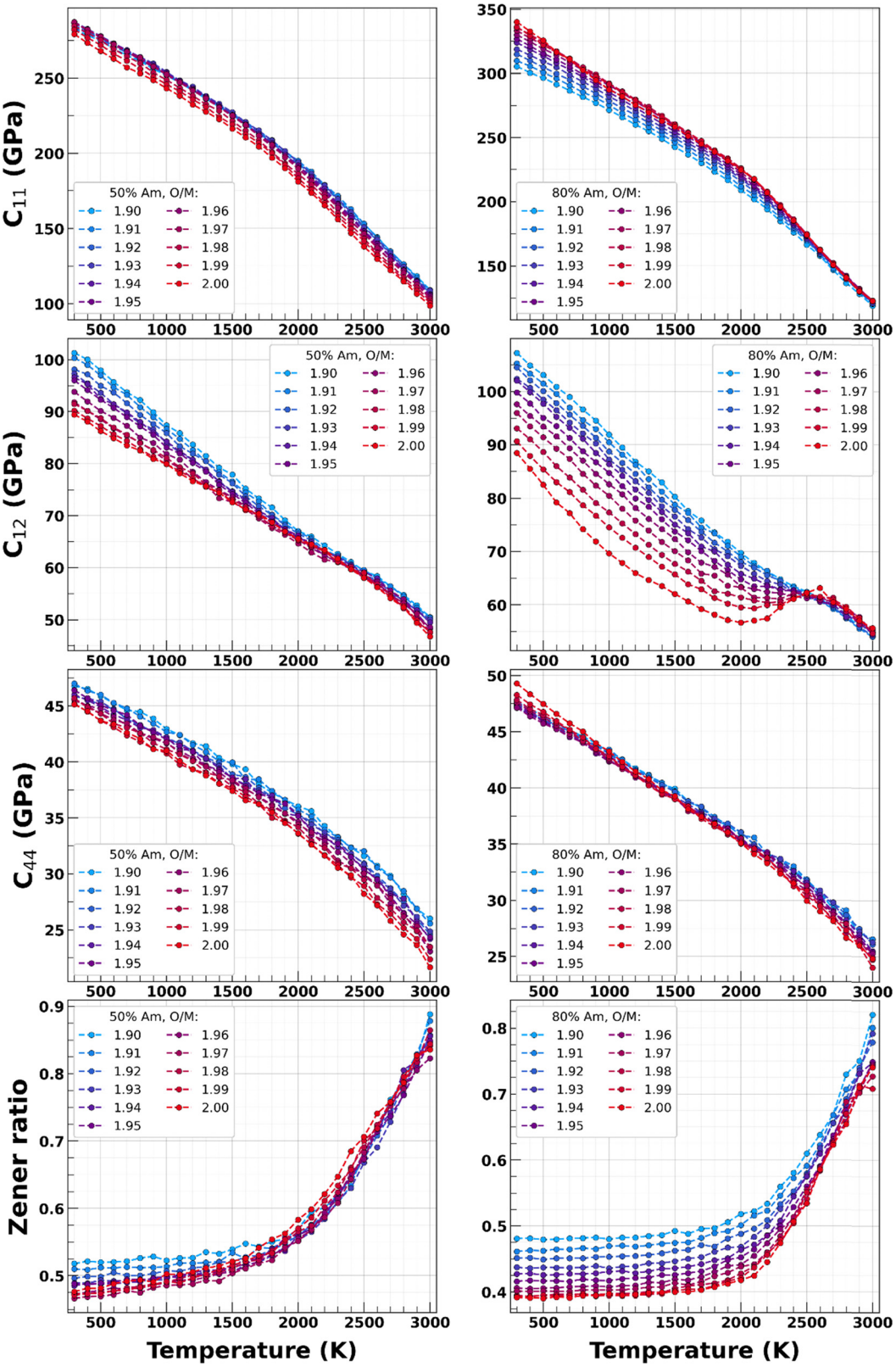

Fig. 18 Evolution with temperature of C_{11}, C_{12}, C_{44} and the Zener ratio for $U_{0.5}Am_{0.5}O_{2-x}$ (left column) and $U_{0.2}Am_{0.8}O_{2-x}$ (right column) for $0 \leq x \leq 0.1$.

Acknowledgements

The authors would like to thank Bruno Michel and Anna Smith for fruitful discussions. This work was supported by the basic research Program (RTA) of the CEA Energy Division and is part of the PATRICIA project, which has received funding from the Euratom research and training programme 2019–2020 under grant agreement no 945077. It was performed using HPC resources from GENCI at TGCC and CINES under the allocations 2023 – A0150906922 and 2023 – R0151010339, as well as resources from CCRT funded by the CEA/DES simulation programme.

References

1 *Homogeneous versus Heterogeneous Recycling of Transuranics in Fast Nuclear Reactors*, Nuclear Energy Agency: Organisation for Economic Co-operation and Development, Paris, 2012.
2 A. Barco, *et al.*, Design and Development of the ESA Am-Fueled Radioisotope Power Systems, *2019 IEEE Aerospace Conference*, Big Sky, MT, USA, 2019, pp. 1–11, DOI: 10.1109/AERO.2019.8741786.
3 A. Barco, C. Fongarland, A. Group and R. M. Ambrosi, Safety Studies for the ESA Space Nuclear Power Systems: Accident Modelling and Analysis, *2019 IEEE Aerospace Conference*, Big Sky, MT, USA, 2019, pp. 1–8, DOI: 10.1109/AERO.2019.8741744.
4 T. Wiss and D. Freis, Investigation on the use of Americium Oxide for Space Power Sources: Radiation Damage Studies, *E3S Web Conf.*, 2017, **16**, 05004.
5 C. Barklay, E. J. Watkinson, R. Ambrosi, R. Mesalam, A. Barco and D. Kramer, Considerations for Utilising Alternative Radioisotopes in Radioisotope Power Systems, *2021 IEEE Aerospace Conference (50100)*, IEEE, Big Sky, MT, USA, 2021, pp. 1–6, DOI: 10.1109/AERO50100.2021.9438353.
6 E. J. Watkinson, *et al.*, Thermal Properties and Behaviour of Am-Bearing Fuel in European Space Radioisotope Power Systems, *Thermo*, 2021, **1**(3), 297–331, DOI: 10.3390/thermo1030020.
7 A. V. Mikhalev, D. O. Chernov and V. V. Korobeinikov, Use of Am-241 in RTGs, *J. Phys.: Conf. Ser.*, 2020, **1689**(1), 012063, DOI: 10.1088/1742-6596/1689/1/012063.
8 J.-F. Vigier, *et al.*, Optimization of Uranium-Doped Americium Oxide Synthesis for Space Application, *Inorg. Chem.*, 2018, **57**(8), 4317–4327, DOI: 10.1021/acs.inorgchem.7b03148.
9 R. Ambrosi, *et al.*, Americium-241 radioisotope thermoelectric generator development for space applications, *International nuclear atlantic conference (INAC 2013), Recife, PE (Brazil), 24-29 Nov 2013*, 2013, https://inis.iaea.org/records/mp9hr-13a17.
10 R. M. Ambrosi, D. P. Kramer, E. J. Watkinson, R. Mesalam and A. Barco, A Concept Study on Advanced Radioisotope Solid Solutions and Mixed-Oxide Fuel Forms for Future Space, *Nucl. Technol.*, 2021, **207**, 773–781.
11 D. Horlait, F. Lebreton, P. Roussel and T. Delahaye, XRD Monitoring of α Self-Irradiation in Uranium–Americium Mixed Oxides, *Inorg. Chem.*, 2013, **52**(24), 14196–14204, DOI: 10.1021/ic402124s.
12 O. S. Vălu, D. Staicu, O. Beneš, R. J. M. Konings and P. Lajarge, Heat capacity, thermal conductivity and thermal diffusivity of uranium–americium mixed oxides, *J. Alloys Compd.*, 2014, **614**, 144–150, DOI: 10.1016/j.jallcom.2014.05.083.
13 D. Prieur, *et al.*, Local Structure and Charge Distribution in Mixed Uranium–Americium Oxides: Effects of Oxygen Potential and Am Content, *Inorg. Chem.*, 2011, **50**(24), 12437–12445, DOI: 10.1021/ic200910f.
14 D. Prieur, *et al.*, Accommodation of multivalent cations in fluorite-type solid solutions: case of Am-bearing UO_2, *J. Nucl. Mater.*, 2013, **434**(1–3), 7–16, DOI: 10.1016/j.jnucmat.2012.11.037.
15 D. Prieur, *et al.*, Melting behaviour of americium-doped uranium dioxide, *J. Chem. Thermodyn.*, 2016, **97**, 244–252, DOI: 10.1016/j.jct.2016.02.003.
16 F. Lebreton, *Synthèse et caractérisation d'oxydes mixtes d'uranium et d'américium*, Université de Limoges, 2014.
17 E. Epifano, *et al.*, High temperature heat capacity of $(U,Am)O_{2\pm x}$, *J. Nucl. Mater.*, 2017, **494**, 95–102, DOI: 10.1016/j.jnucmat.2017.07.009.
18 E. Epifano, *et al.*, Extreme multi-valence states in mixed actinide oxides, *Commun. Chem.*, 2019, **2**(1), 59, DOI: 10.1038/s42004-019-0161-0.
19 E. Epifano, *et al.*, Behaviour of $(U,Am)O_2$ in oxidizing conditions: a high-temperature XRD study, *J. Nucl. Mater.*, 2020, **531**, 151991, DOI: 10.1016/j.jnucmat.2020.151991.
20 E. Epifano, *et al.*, Melting behaviour of uranium–americium mixed oxides under different atmospheres, *J. Chem. Thermodyn.*, 2020, **140**, 105896, DOI: 10.1016/j.jct.2019.105896.
21 E. Epifano, *Study of the U–Am–O ternary phase diagram*, Université Paris-Saclay, 2017.
22 M. Bertolus and B. Michel, *D7.6 Synthesis of INSPYRE results*, INSPYRE Deliverables, 2022.
23 M. Bertolus, *et al.*, Linking atomic and mesoscopic scales for the modelling of the transport properties of uranium dioxide under irradiation, *J. Nucl. Mater.*, 2015, **462**, 475–495, DOI: 10.1016/j.jnucmat.2015.02.026.
24 M. W. D. Cooper, M. J. D. Rushton and R. W. Grimes, A many-body potential approach to modelling the thermomechanical properties of actinide oxides, *J. Phys.: Condens. Matter*, 2014, **26**(10), 105401, DOI: 10.1088/0953-8984/26/10/105401.
25 M. W. D. Cooper, S. T. Murphy, M. J. D. Rushton and R. W. Grimes, Thermophysical properties and oxygen transport in the $(U_x,Pu_{1-x})O_2$ lattice, *J. Nucl. Mater.*, 2015, **461**, 206–214, DOI: 10.1016/j.jnucmat.2015.03.024.
26 M. W. D. Cooper, S. T. Murphy, P. C. M. Fossati, M. J. D. Rushton and R. W. Grimes, Thermophysical and anion diffusion properties of $(U_x,Th_{1-x})O_2$, *Proc. Phys. Soc., London, Sect. A*, 2014, **470**(2171), 20140427, DOI: 10.1098/rspa.2014.0427.
27 M. J. Rahman, B. Szpunar and J. A. Szpunar, Comparison of thermomechanical properties of $(U_x,Th_{1-x})O_2$, $(U_x,Pu_{1-x})O_2$ and $(Pu_x,Th_{1-x})O_2$ systems, *J. Nucl. Mater.*, 2019, **513**, 8–15, DOI: 10.1016/j.jnucmat.2018.10.038.
28 P. S. Ghosh, *et al.*, Melting behavior of $(Th,U)O_2$ and $(Th,Pu)O_2$ mixed oxides, *J. Nucl. Mater.*, 2016, **479**, 112–122, DOI: 10.1016/j.jnucmat.2016.06.037.

29 C. O. T. Galvin, M. Machida, H. Nakamura, D. A. Andersson and M. W. D. Cooper, Correlations for the specific heat capacity of $(U_xPu_{1-x})1 - yGd_yO_{2-z}$ derived from molecular dynamics, *J. Nucl. Mater.*, 2022, **572**, 154028, DOI: 10.1016/j.jnucmat.2022.154028.

30 C. O. T. Galvin, P. A. Burr, M. W. D. Cooper, P. C. M. Fossati and R. W. Grimes, Using molecular dynamics to predict the solidus and liquidus of mixed oxides $(Th,U)O_2$, $(Th,Pu)O_2$ and $(Pu,U)O_2$, *J. Nucl. Mater.*, 2020, **534**, 152127, DOI: 10.1016/j.jnucmat.2020.152127.

31 I. Cheik Njifon and E. Torres, Phonons and thermophysical properties of $U_{1-x}Pu_xO_2$ mixed oxide (MOX) fuels, *J. Nucl. Mater.*, 2020, **537**, 152158, DOI: 10.1016/j.jnucmat.2020.152158.

32 C. Takoukam-Takoundjou, E. Bourasseau and V. Lachet, Study of thermodynamic properties of $U_{1-y}Pu_yO_2$ MOX fuel using classical molecular Monte Carlo simulations, *J. Nucl. Mater.*, 2020, **534**, 152125, DOI: 10.1016/j.jnucmat.2020.152125.

33 C. Takoukam-Takoundjou, E. Bourasseau, M. J. D. Rushton and V. Lachet, Optimization of a new interatomic potential to investigate the thermodynamic properties of hypo-stoichiometric mixed oxide fuel $U_{1-y}Pu_yO_{2-x}$, *J. Phys.: Condens. Matter*, 2020, **32**(50), 505702, DOI: 10.1088/1361-648X/abace3.

34 E. Jossou, L. Malakkal, J. Ranasingh, B. Szpunar and J. Szpunar, Thermophysical properties of $(U_xAm_{1-x})O_2$ MOX fuel, *Comput. Mater. Sci.*, 2020, **172**, 109324, DOI: 10.1016/j.commatsci.2019.109324.

35 D. Bathellier, M. Lainet, M. Freyss, P. Olsson and E. Bourasseau, A new heat capacity law for UO_2, PuO_2 and $(U,Pu)O_2$ derived from molecular dynamics simulations and useable in fuel performance codes, *J. Nucl. Mater.*, 2021, **549**, 152877, DOI: 10.1016/j.jnucmat.2021.152877.

36 M. J. D. Rushton and A. Chroneos, Impact of uniaxial strain and doping on oxygen diffusion in CeO_2, *Sci. Rep.*, 2014, **4**(1), 6068, DOI: 10.1038/srep06068.

37 X.-Y. Liu, *et al.*, Molecular Dynamics Simulation of Thermal Transport in UO_2 Containing Uranium, Oxygen, and Fission-product Defects, *Phys. Rev. Appl.*, 2016, **6**(4), 044015, DOI: 10.1103/PhysRevApplied.6.044015.

38 B. Labonne, S. Orlat and M. Bertolus, Development of an interatomic potential for mixed uranium–americium oxides and application to the determination of the structural and thermodynamic properties of $(U,Am)O_2$ with americium contents below 50%, *J. Nucl. Mater.*, 2023, **579**, 154390, DOI: 10.1016/j.jnucmat.2023.154390.

39 S. Casalta, Etude des propriétés du système Am-O en vue de la transmutation de l'Americium 241 en réacteur à neutrons rapides, *Thèse Aix-Marseille I*, 1996, https://theses.fr/1996AIX11036.

40 M. Kato, K. Morimoto, H. Sugata, K. Konashi, M. Kashimura and T. Abe, Solidus and liquidus temperatures in the UO_2–PuO_2 system, *J. Nucl. Mater.*, 2008, **373**(1–3), 237–245, DOI: 10.1016/j.jnucmat.2007.06.002.

41 M. S. Daw and M. I. Baskes, Semiempirical, Quantum Mechanical Calculation of Hydrogen Embrittlement in Metals, *Phys. Rev. Lett.*, 1983, **50**(17), 1285–1288, DOI: 10.1103/PhysRevLett.50.1285.

42 M. S. Daw and M. I. Baskes, Embedded-atom method: derivation and application to impurities, surfaces, and other defects in metals, *Phys. Rev. B: Condens. Matter Mater. Phys.*, 1984, **29**(12), 6443–6453, DOI: 10.1103/PhysRevB.29.6443.

43 P. M. Morse, Diatomic Molecules According to the Wave Mechanics. II. Vibrational Levels, *Phys. Rev.*, 1929, **34**(1), 57–64, DOI: 10.1103/PhysRev.34.57.

44 R. A. Buckingham, The classical equation of state of gaseous helium, neon and argon, *Proc. Phys. Soc., London, Sect. A*, 1938, **168**(933), 264–283, DOI: 10.1098/rspa.1938.0173.

45 M. S. Talla Noutack, G. Jomard, M. Freyss and G. Geneste, Structural, electronic and energetic properties of uranium–americium mixed oxides $U_{1-y}Am_{y2}$ using DFT+*U* calculations, *J. Phys.: Condens. Matter*, 2019, **31**(48), 485501, DOI: 10.1088/1361-648X/ab395e.

46 M. S. T. Noutack, M. Freyss, G. Jomard and G. Geneste, Electron polarons and donor point defects in americium dioxide AmO_2, *Phys. Rev. B*, 2020, **101**(2), 024108, DOI: 10.1103/PhysRevB.101.024108.

47 A. P. Thompson, *et al.*, LAMMPS – a flexible simulation tool for particle-based materials modeling at the atomic, meso, and continuum scales, *Comput. Phys. Commun.*, 2022, **271**, 108171, DOI: 10.1016/j.cpc.2021.108171.

48 P. Carnevali, F. Ercolessi and E. Tosatti, Melting and non-melting behavior of the Au(111) surface, *Phys. Rev. B: Condens. Matter Mater. Phys.*, 1987, **36**(12), 6701–6704, DOI: 10.1103/PhysRevB.36.6701.

49 F. Ercolessi, W. Andreoni and E. Tosatti, Melting of small gold particles: mechanism and size effects, *Phys. Rev. Lett.*, 1991, **66**(7), 911–914, DOI: 10.1103/PhysRevLett.66.911.

50 J. R. Morris, C. Z. Wang, K. M. Ho and C. T. Chan, Melting line of aluminum from simulations of coexisting phases, *Phys. Rev. B: Condens. Matter Mater. Phys.*, 1994, **49**(5), 3109–3115, DOI: 10.1103/PhysRevB.49.3109.

51 A. B. Belonoshko, Molecular dynamics of $MgSiO_3$ perovskite at high pressures: equation of state, structure, and melting transition, *Geochim. Cosmochim. Acta*, 1994, **58**(19), 4039, DOI: 10.1016/0016-7037(94)90265-8.

52 F. Cricchio, A. B. Belonoshko, L. Burakovsky, D. L. Preston and R. Ahuja, High-pressure melting of lead, *Phys. Rev. B: Condens. Matter Mater. Phys.*, 2006, **73**(14), 140103, DOI: 10.1103/PhysRevB.73.140103.

53 J. Bouchet, F. Bottin, G. Jomard and G. Zérah, Melting curve of aluminum up to 300 GPa obtained through *ab initio* molecular dynamics simulations, *Phys. Rev. B: Condens. Matter Mater. Phys.*, 2009, **80**(9), 094102, DOI: 10.1103/PhysRevB.80.094102.

54 W. Voigt, *Lehrbuch der Kristallphysik*, 1928, vol. 962.

55 A. Reuss, *Z. Angew. Math. Mech.*, 1929, **9**, 55.

56 R. Hill, The Elastic Behaviour of a Crystalline Aggregate, *Proc. Phys. Soc., London, Sect. A*, 1952, **65**, 349.

57 R. E. McHenry, Melting Points of Curium and Americium Oxides, *Trans. Am. Nucl. Soc.*, 1965, **8**, 75.

58 E. Epifano, *et al.*, Insight into the Am–O Phase Equilibria: A Thermodynamic Study Coupling High-Temperature XRD and CALPHAD Modeling, *Inorg. Chem.*, 2017, **56**(13), 7416–7432, DOI: 10.1021/acs.inorgchem.7b00572.

59 P. Gotcu-Freis, J.-Y. Colle, C. Guéneau, N. Dupin, B. Sundman and R. J. M. Konings, A thermodynamic study of the Pu–Am–O system, *J. Nucl. Mater.*, 2011, **414**(3), 408–421, DOI: 10.1016/j.jnucmat.2011.05.014.

60 M. Rochedy, A. L. Smith, M. Bertolus, B. Labonne, C. Guéneau and O. Beneš, D4.3 Measurements and atomic scale calculations in U–Pu–Am–Np–O systems, *PATRICIA Deliverable*, 2023, https://cordis.europa.eu/project/id/945077/results/en.

61 C. Guéneau, A. Chartier, P. Fossati, L. Van Brutzel and P. Martin, Thermodynamic and Thermophysical Properties of the Actinide Oxides, *Comprehensive Nuclear Materials*, Elsevier, 2020, pp. 111–154, DOI: 10.1016/B978-0-12-803581-8.11786-2.

62 R. J. M. Konings, *et al.*, The Thermodynamic Properties of the f-Elements and their Compounds. Part 2. The Lanthanide and Actinide Oxides, *J. Phys. Chem. Ref. Data*, 2014, **43**(1), 013101, DOI: 10.1063/1.4825256.

63 I. D. Prodan, G. E. Scuseria and R. L. Martin, Covalency in the actinide dioxides: systematic study of the electronic properties using screened hybrid density functional theory, *Phys. Rev. B: Condens. Matter Mater. Phys.*, 2007, **76**(3), 033101, DOI: 10.1103/PhysRevB.76.033101.

64 L. Petit, A. Svane, Z. Szotek, W. M. Temmerman and G. M. Stocks, Electronic structure and ionicity of actinide oxides from first principles, *Phys. Rev. B: Condens. Matter Mater. Phys.*, 2010, **81**(4), 045108, DOI: 10.1103/PhysRevB.81.045108.

65 B. M. Adams, *et al.*, Dakota, A Multilevel Parallel Object-Oriented Framework for Design Optimization, Parameter Estimation, Uncertainty Quantification, and Sensitivity Analysis: Version 6.15 User's Manual, Sandia Technical Report, SAND2020-12495, 2021.

66 Eddy and John, JEGA V 2.3, 2009.

67 J. A. Fahey, R. P. Turcotte and T. D. Chikalla, Thermal expansion of the actinide dioxides, *Inorg. Nucl. Chem. Lett.*, 1974, **10**(6), 459–465, DOI: 10.1016/0020-1650(74)80067-X.

68 M. Idiri, T. Le Bihan, S. Heathman and J. Rebizant, Behavior of actinide dioxides under pressure: UO_2 and ThO_2, *Phys. Rev. B: Condens. Matter Mater. Phys.*, 2004, **70**(1), 014113, DOI: 10.1103/PhysRevB.70.014113.

69 T. Nishi, A. Itoh, K. Ichise and Y. Arai, Heat capacities and thermal conductivities of AmO_2 and $AmO_{1.5}$, *J. Nucl. Mater.*, 2011, **414**(2), 109–113, DOI: 10.1016/j.jnucmat.2011.01.019.

70 M. S. Talla Noutack, G. Geneste, G. Jomard and M. Freyss, First-principles investigation of the bulk properties of americium dioxide and sesquioxides, *Phys. Rev. Mater.*, 2019, **3**(3), 035001, DOI: 10.1103/PhysRevMaterials.3.035001.

71 W. Huang and H. Chen, Investigation of the elastic, hardness, and thermodynamic properties of actinide oxides, *Phys. B*, 2014, **449**, 133–137, DOI: 10.1016/j.physb.2014.05.024.

72 Y. Lu, Y. Yang, F. Zheng, B.-T. Wang and P. Zhang, Electronic, mechanical, and thermodynamic properties of americium dioxide, *J. Nucl. Mater.*, 2013, **441**(1–3), 411–420, DOI: 10.1016/j.jnucmat.2013.06.043.

73 E. Caglak and P.-E. Labeau, Lattice parameter of Am, Np bearing MOX fuel: an empirical potential study, *J. Phys. Commun.*, 2021, **5**(3), 035012, DOI: 10.1088/2399-6528/abe921.

74 M. Rochedy, A. Smith, M. Bertolus, B. Labonne, C. Guéneau and O. Benes, D4.4 Final report on thermodynamic models of U-Pu-Am-Np-O systems, PATRICIA H2020 Deliverable, to be published 2024.

75 D. S. Aidhy, B. Liu, Y. Zhang and W. J. Weber, Chemical expansion affected oxygen vacancy stability in different oxide structures from first principles calculations, *Comput. Mater. Sci.*, 2015, **99**, 298–305, DOI: 10.1016/j.commatsci.2014.12.030.

76 R. A. Hein and P. N. Flagella, Technical Report GEMP-578, 1968, DOI: 10.2172/4552169.

77 L. Leibowitz, L. W. Mishler and M. G. Chasanov, Enthalpy of solid uranium dioxide from 2500 °K to its melting point, *J. Nucl. Mater.*, 1969, **29**(3), 356.

78 A. E. Ogard, Plutonium 1970 and Other Actinides, *Metallurgical Society of the American Institute of Mining*, 1970, p. 78.

79 P. Fouquet-Métivier, *et al.*, Investigation of the solid/liquid phase transitions in the U–Pu–O system, *Calphad*, 2023, **80**, 102523, DOI: 10.1016/j.calphad.2022.102523.

80 A. S. Dworkin and M. A. Bredig, Diffuse transition and melting in fluorite and antifluorite type of compounds. Heat content of potassium sulfide from 298 to 1260 degree K, *J. Phys. Chem.*, 1968, **72**(4), 1277–1281, DOI: 10.1021/j100850a035.

81 M. T. Hutchings, High-temperature studies of UO_2 and ThO_2 using neutron scattering techniques, *J. Chem. Soc., Faraday Trans. 2*, 1987, **83**(7), 1083, DOI: 10.1039/f29878301083.

82 J. Ralph and G. J. Hyland, Empirical confirmation of a bredig transition in UO_2, *J. Nucl. Mater.*, 1985, **132**, 76.

83 J. P. Hiernaut, G. J. Hyland and C. Ronchi, Premelting transition in uranium dioxide, *Int. J. Thermophys.*, 1993, **14**, 609–612, DOI: 10.1007/BF00566058.

84 T. R. Pavlov, *et al.*, Measurement and interpretation of the thermo-physical properties of UO_2 at high temperatures: the viral effect of oxygen defects, *Acta Mater.*, 2017, **139**, 138–154, DOI: 10.1016/j.actamat.2017.07.060.

85 C. Ronchi, J. P. Hiernaut and G. J. Hyland, Laboratory Measurement of the Heat Capacity of Urania up to 8000 K: I. Experiment, *Nucl. Sci. Eng.*, 1993, **113**(1), 1.

86 C. B. Basak, A. K. Sengupta and H. S. Kamath, Classical molecular dynamics simulation of UO_2 to predict thermophysical properties, *J. Alloys Compd.*, 2003, **360**(1–2), 210–216, DOI: 10.1016/S0925-8388(03)00350-5.

87 E. Yakub, C. Ronchi and D. Staicu, Molecular dynamics simulation of premelting and melting phase transitions in stoichiometric uranium dioxide, *J. Chem. Phys.*, 2007, **127**(9), 094508, DOI: 10.1063/1.2764484.

88 S. I. Potashnikov, A. S. Boyarchenkov, K. A. Nekrasov and A. Y. Kupryazhkin, High-precision molecular dynamics simulation of UO_2–PuO_2: pair potentials comparison in UO_2, *J. Nucl. Mater.*, 2011, **419**(1–3), 217–225, DOI: 10.1016/j.jnucmat.2011.08.033.

89 E. T. Dubois, J. Tranchida, J. Bouchet and J.-B. Maillet, Atomistic simulations of nuclear fuel UO_2 with machine learning interatomic potentials, *Phys. Rev. Mater.*, 2024, **8**(2), 025402, DOI: **10.1103/PhysRevMaterials.8.025402**.

90 D. Bathellier, M. Freyss, I. Cheik Njifon, P. Olsson, E. Bourasseau and M. Bertolus, Heat capacity of UO_2 and PuO_2 from ab initio molecular dynamics simulations, To be published.

91 A. Annamareddy and J. Eapen, Low Dimensional String-like Relaxation Underpins Superionic Conduction in Fluorites and Related Structures, *Sci. Rep.*, 2017, **7**(1), 44149, DOI: **10.1038/srep44149**.

92 H. Zhang, X. Wang, A. Chremos and J. F. Douglas, Superionic UO_2: a model anharmonic crystalline material, *J. Chem. Phys.*, 2019, **150**(17), 174506, DOI: **10.1063/1.5091042**.

93 P. C. M. Fossati, A. Chartier and A. Boulle, Structural Aspects of the Superionic Transition in AX_2 Compounds With the Fluorite Structure, *Front. Chem.*, 2021, **9**, 723507, DOI: **10.3389/fchem.2021.723507**.

94 G. Porto, *et al.*, Thermodynamic and thermoelastic properties of hypostoichiometric MOX fuels with molecular dynamics simulations, *J. Nucl. Mater.*, 2024, **598**, 155163, DOI: **10.1016/j.jnucmat.2024.155163**.